3.4.1. “CORONAS-F”

The CORONAS space mission (Complex orbital near-Earth observations of solar activity) forms part of a long-term solar-terrestrial research program developed and carried out by the Division of Physical Sciences, Council on Space, and Scientific Council on Solar-Terrestrial Physics of the Russian Academy of Sciences within the frames of the Space Program of Russian Federation under the auspices of the Federal Space Agency. The mission comprises a series of three satellites: CORONAS-I (active operation from 1994 to 2001), “CORONAS-F” (active operation from July 31, 2001 to December 6, 2005, orbital height 400–500 km, inclination ~83° (Figs. 1, 2) and the satellite to be launched CORONAS-PHOTON.

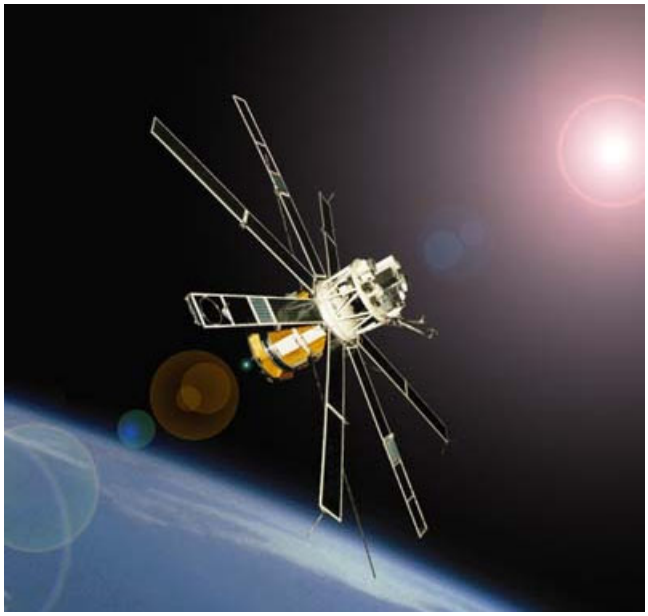

Fig. 1. Satellite “CORONAS-F” in orbit

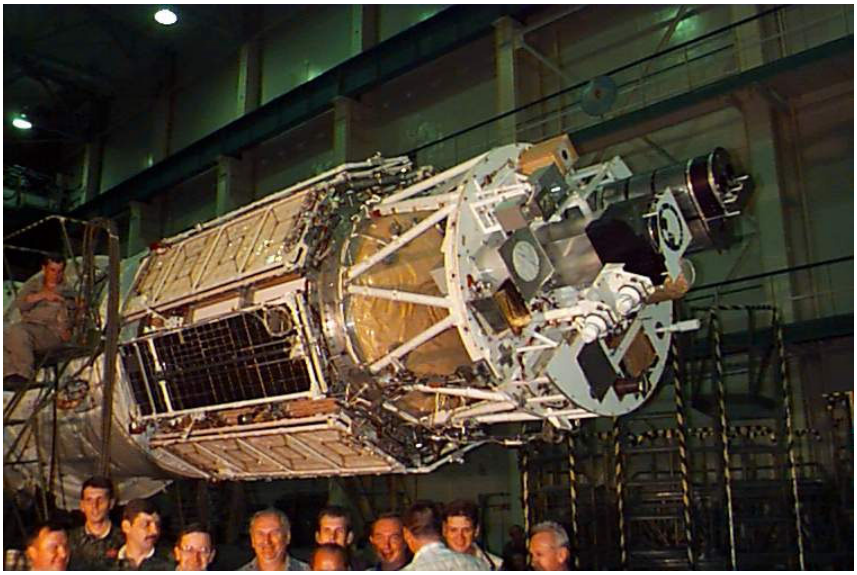

Fig. 2. Satellite “CORONAS-F” docked to the Cyclon missile

"CORONAS-I" was studying the rise phase of the current solar activity cycle 23 (Fig. 3), and the next satellite "CORONAS-F" started observations at the maximum of the cycle and continued them until December 6, 2004, when it ceased to exist as a result of natural evolution of the orbit.

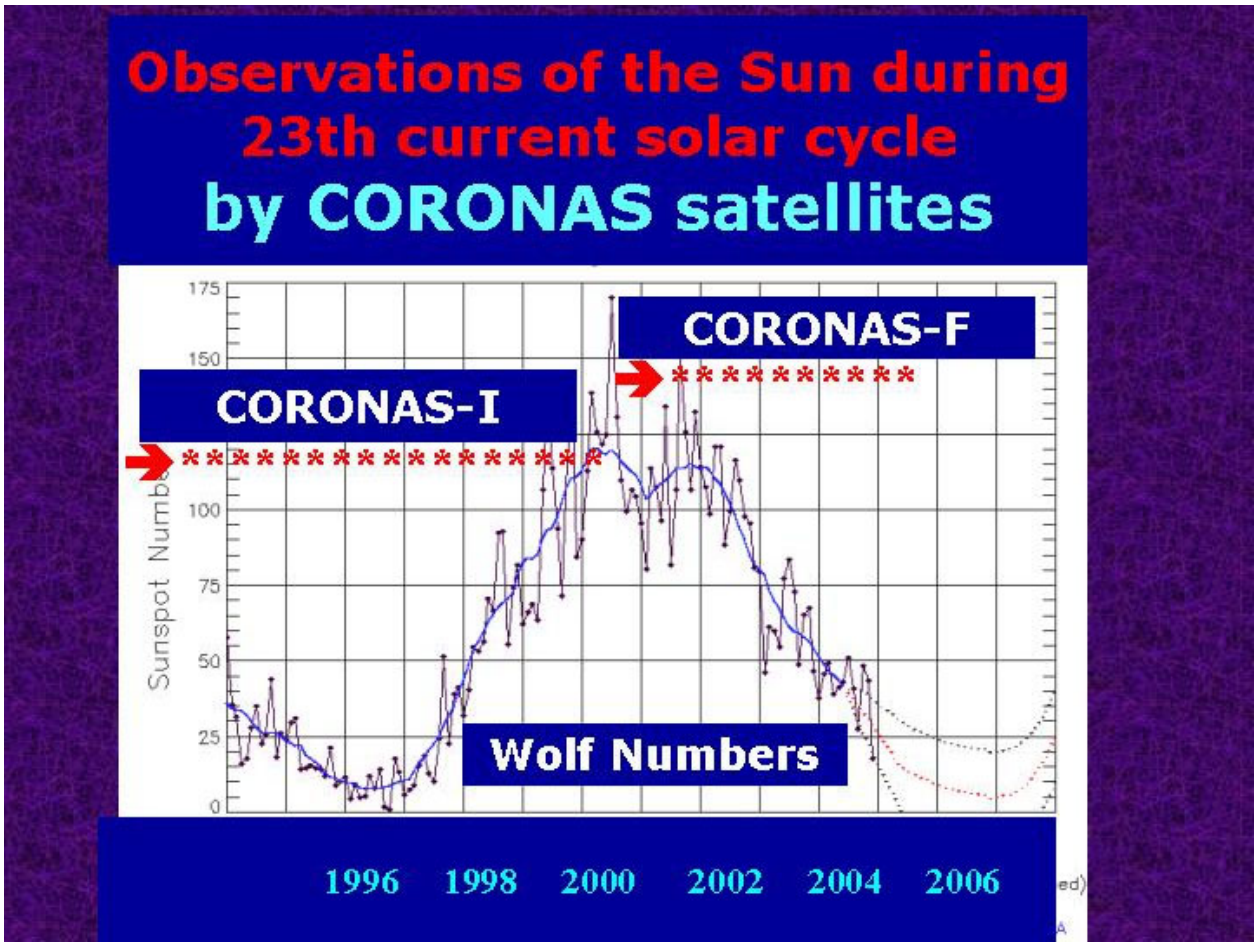

Fig. 3. Observations of the current activity cycle 23 with the "CORONAS-I" and "CORONAS-F" satellites

"*CORONAS-F*" *scientific payload and measuring ranges*

The scientific payload of the "CORONAS-F" mission (Fig. 4) comprised 15 devices. Thus, it was a space solar observatory operating in the autonomous regime and controlled from the ground. The complex of the onboard scientific instruments was controlled from the Flight Control Center, IZMIRAN. The complex carried out observations of the Sun in the entire electromagnetic spectrum from optical to gamma radiation (Table 1). The data obtained allow a comprehensive analysis of the solar phenomena and solar-terrestrial coupling.

Fig. 4. Scientific payload of "CORONAS-F"

Helioseismic observations. DIFOS experiment

Continuous helioseismic observations with a Multi-Channel Spectrophotometer DIFOS started on board the CORONAS-F satellite on August 15, 2001. The device recorded low ($l = 0, 1, 2$) eigenmodes of global oscillations of the Sun (acoustic-type oscillations with a period of about 5 min called *p*-modes) in a broad wavelength range from 350 to 1500 nm and measured minor variations of the solar irradiance (10^{-5}…10^{-6} of the total flux) associated with these oscillations. An important result of those observations was that they showed the feasibility of helioseismic studies based on observations at the Earth's orbit. Such studies became possible owing to the newly developed methods that allowed us to fill the gaps in data in the periods of crossing the Earth's shadow, to subtract the light reflected from the Earth's atmosphere and detected by the spectrophotometer, to analyze the data obtained and compare them with the results of other observations and theoretical investigations. Figure 5 illustrates the power spectrum of the p-modes of global oscillations of the Sun. Each peak in the spectrum corresponds to a harmonic global oscillation (*p*-mode) with a definite period and values l and n (the number of the oscillation nodes in azimuth and radius of the Sun, respectively). At every instant, the device recorded simultaneously from 10 to 15 harmonics. These harmonics are excited at random instants, exist for a few days or weeks, and then, disappear giving way to the newly excited harmonics with different periods.

Table 1. Scientific instruments of "CORONAS-F" and their measuring ranges

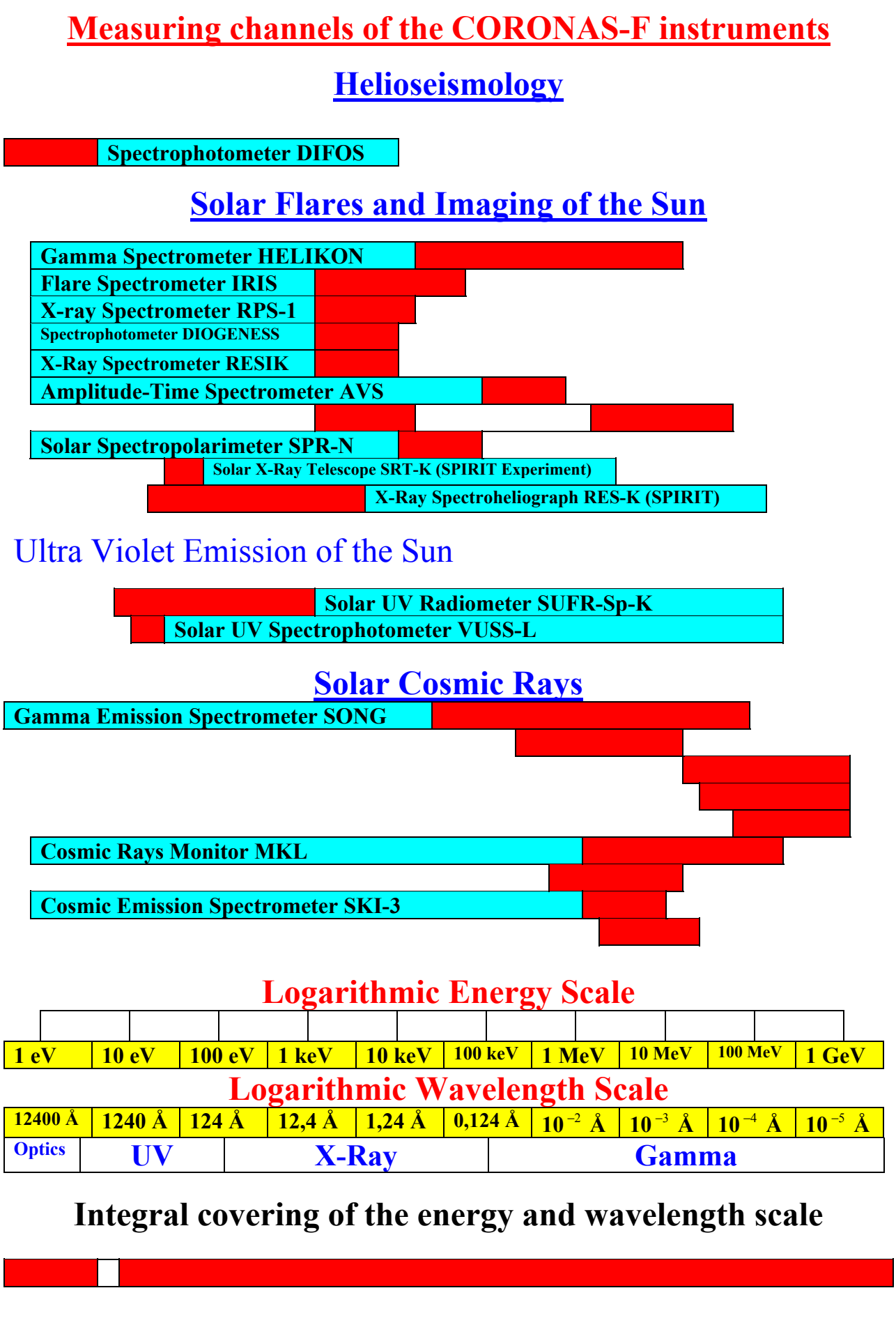

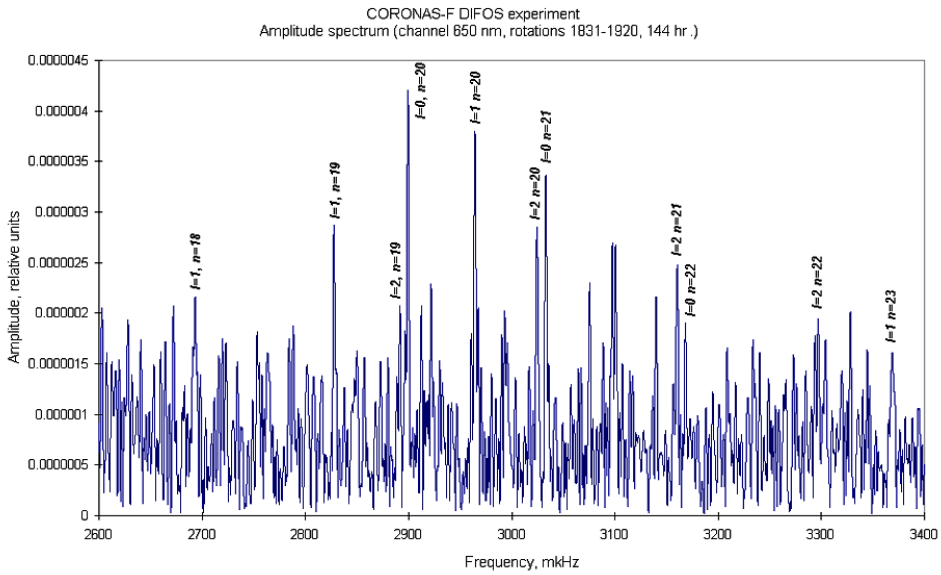

Fig. 5. Power spectrum of the global oscillations of the Sun. DIFOS/CORONAS-F experiment

The DIFOS data were used to perform an amplitude-frequency-phase analysis of global oscillations by the method of analytical signal, in particular, to determine the instantaneous frequency, amplitude, and phase of the individual *p*-modes at different photospheric levels. It was shown that the broadening of the spectral lines of the oscillation *p*-modes occurred mainly due to the fluctuation of the oscillation amplitude, while the oscillation frequency remained stable $\sim 10^{-4}$. This corresponds to the spectral line broadening by no more than 0.4 MHz or the time scale of frequency variations of the order of a month. The multiple channels of the DIFOS spectrophotometer (350, 500, 650, 850, 1100, and 1500 nm), which distinguish it significantly from other space-borne devices recording fluctuations of the solar luminosity, allowed us to examine the phase shift of the oscillations observed in different channels (Figs. 6, 7) and to reveal a previously unknown effect: the motion of oscillations from the upper and lower to the middle layers of the photosphere. The fact that oscillations move downward from the upper photosphere, while their source is under the photosphere in the convection zone, cannot be explained in terms of the adiabatic theory usually applied to helioseismic observations. Therefore, the explanation must be sought for in terms of the non-adiabatic theory describing oscillations in the photosphere. The waves run to the middle of the photosphere where the oscillation damping is the strongest due to the non-adiabaticity, which is caused by a high efficiency of the radiative heat transfer and low relaxation time of temperature fluctuations. Thus, the middle layers ensure a sink of the energy carried by the waves from above and below. This newly found effect is a direct evidence of non-adiabaticity of the evanescent *p*-modes of oscillations in the photosphere. This property could be revealed owing to the DIFOS experiment, which was the only helioseismic experiment that allowed simultaneous observations of global oscillations of the Sun in different regions of the continuum formed all over the photosphere from the temperature minimum to the deepest layers, where the 1500 nm emission is generated.

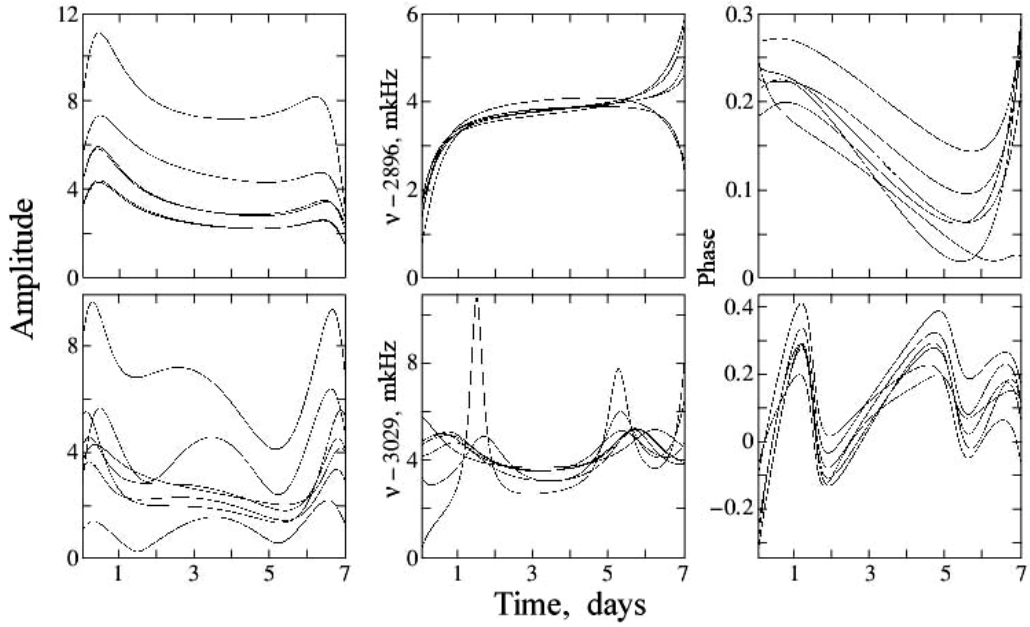

Fig. 6. Instantaneous amplitude (10^{-5} of the mean solar radiation flux in the corresponding channel of the spectrophotometer), excess of instantaneous frequency (μHz) over 2896 and 3029, and phase shifts (radians) of the optical channels 350, 500, 650, and 850 nm with respect to the 1500-nm channel. The upper row shows the plots for the mode $l = 0$, $n = 20$ and the lower one, for $l = 0$, $n = 21$

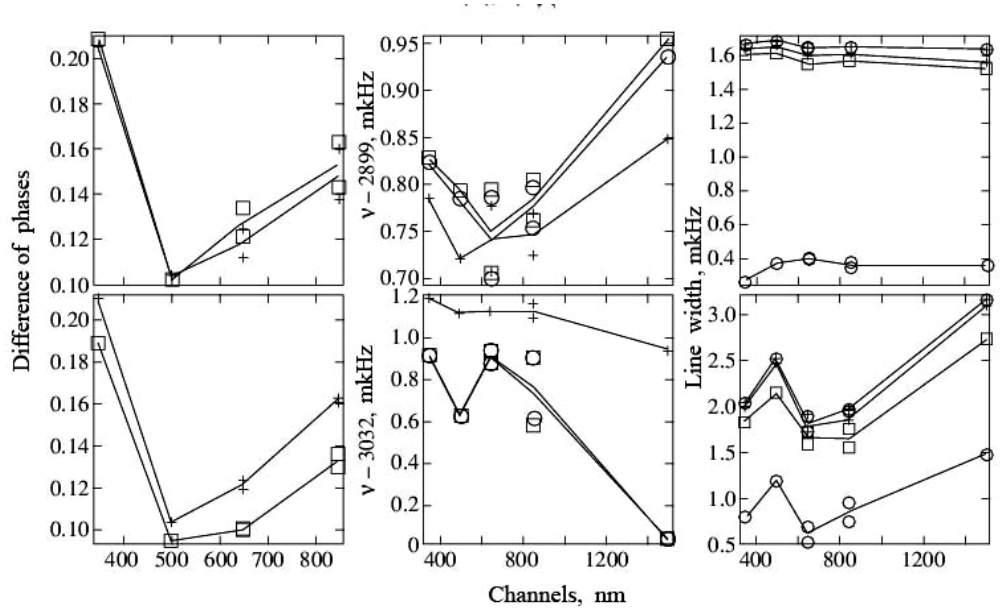

Fig. 7. Averaged parameters of the modes $n = 20$ (upper row) and $n = 21$ (lower row). The left column presents the phase differences between the channels 350, 500, 650, and 850 nm and the channel 1500 nm. The squares denote the differences of the time-averaged instantaneous phases $\Phi(t)$ and the crosses, the phase differences at the maxima of the continuous spectra in the corresponding channels. The middle column provides the mean instantaneous frequency $\langle\omega(t)\rangle$ (squares) and the frequency $\langle\omega\rangle$ averaged over the spectrum (crosses). The circles denote the frequencies of the maxima of the continuous spectra in the corresponding channels. The right column contains the total line widths determined directly from the spectrum (circles) and with the use of the analytical signal (crosses), as well as the contribution of the amplitude (squares) and frequency (crossed circles) modulation to the total line width

Using as an example the oscillation mode with $l = 0$, $n = 21$, we have separated the measured signals with close frequencies by the analytical signal method and showed reliably that the signal of this mode contains, besides the principal harmonic, a second one with an amplitude three times smaller and a frequency differing from the principal harmonic only by 2.3 μHz. The asymmetry of the oscillation spectrum in Fig. 8 is rather associated with the presence of the second harmonic than with the asymmetric spectrum of the mode $n = 21$ itself. Fig. 9 illustrates the results of separation of the harmonics of mode $n = 21$ for all optical channels of the DIFOS device. The squares in Fig. 9a denote the frequencies of mode $n = 21$ after the harmonic separation. The crosses show for comparison the frequencies of mode $n = 21$ before the harmonic separation determined by averaging the instantaneous frequency and by averaging over the spectrum. The frequencies of the spurious mode denoted with crossed squares proved to be, on the average, smaller than the frequencies of mode $n = 21$ by 3 μHz. The relative amplitude of the spurious mode increases from 0.3 to 0.7 when passing from the 350-nm channel to the 1500-nm one (see Fig. 9b), which corresponds to going from the top to the bottom of the photosphere.

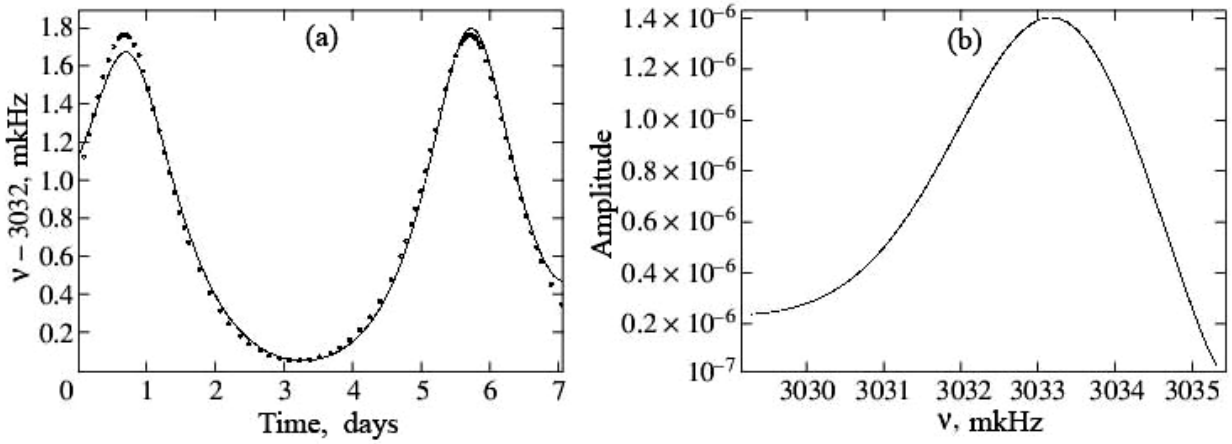

Fig. 8. (a) Time dependence of the instantaneous frequency (solid line) and (b) the mode spectrum demonstrating a high sensitivity of the instantaneous frequency to a weak additional signal component for mode n=21 as measured in the 850-nm channel. The dotted line on panel (a) represents the calculated instantaneous frequency

Solar X-ray images

High-resolution solar images in the spectral lines corresponding to various temperature layers in the solar atmosphere obtained with the solar X-ray Telescope (SPIRIT experiment) made it possible to localize numerous active events on the Sun and to study their morphology. Figure 10 illustrates the solar activity conditions in October and November 2003, when the activity level was higher than ever observed during the past decades. A series of flares of extraordinarily high intensity recorded in that period was accompanied by powerful ejections at a speed up to 2000 km/s. All those events were detected by “CORONAS-F”. The Sun was covered with active regions, numerous magnetic loops, and very hot features. The outstanding flares and ejections recorded in the period under discussion might have

been due to the global (actually, hemispheric) asymmetry of the active regions on the solar surface. The solar images in Fig. 10 obtained at half-rotation intervals show that about 30 active regions existed in one hemisphere and none at all, in another. As a result, large gradients of the magnetic field caused the observed powerful events, which produced strong magnetic storms on the Earth and enhanced cosmic-ray fluxes in near-Earth space.

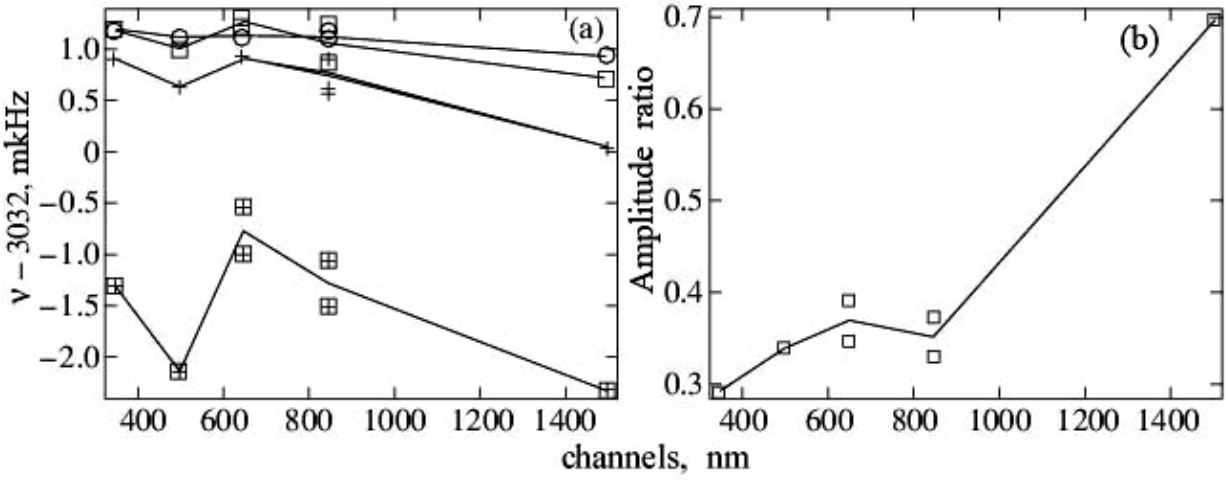

Fig. 9. Results of the harmonic separation of mode $n = 21$ for all optical channels of DIFOS. The squares on panel (a) denote the frequencies of mode $n = 21$ after the harmonic separation; the crosses show the mean frequencies $\langle\omega(t)\rangle$ (instantaneous) and $\langle\omega\rangle$ (averaged over the spectrum) before the harmonic separation. The squares and crossed squares show the high- and low-frequency harmonics of the two-component signal. The circles denote the frequencies corresponding to the maxima of the continuous oscillation spectra in each DIFOS channel. Panel (b) illustrates the amplitude ratio for the spurious mode and mode $n = 21$

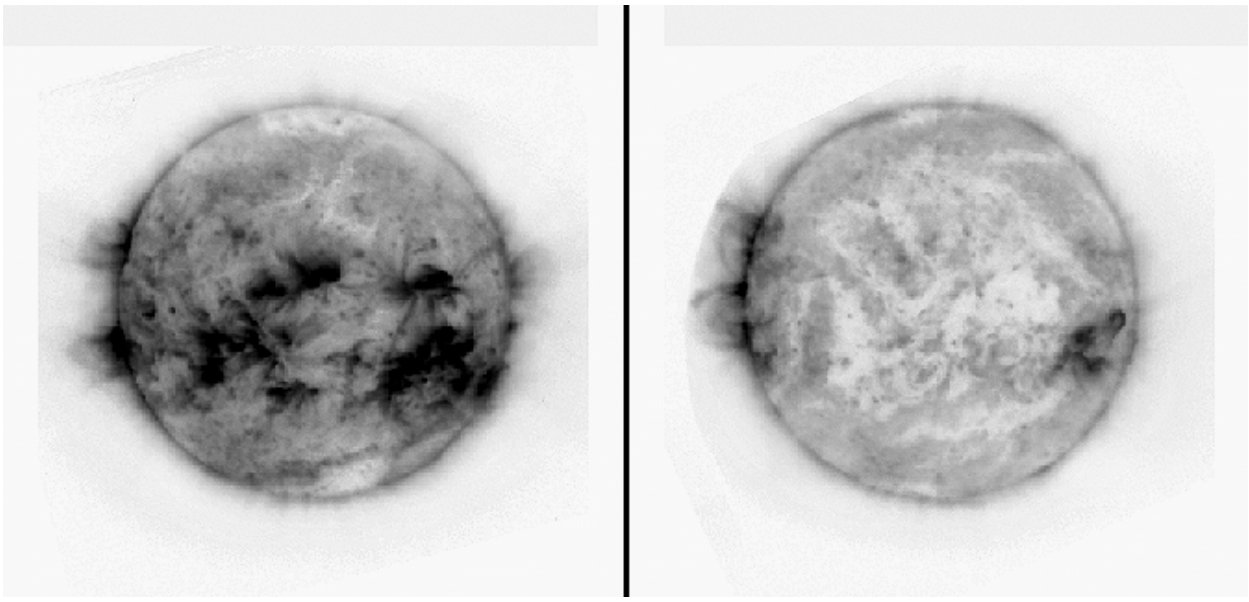

Fig. 10. Solar activity in October and November 2003, when the most intensive events for the past decades were observed on the Sun. One can see the longitudinal (hemispheric) asymmetry in the distribution of active regions over the solar surface

X-ray observations were used to study the global morphology of solar activity in the period of October and November 2003 — the so-called “dimmings” (Fig. 11), which formed as a result of full or partial opening of the initially closed magnetic fields in the process of the coronal mass ejections and the associated decrease of the emission measure. The ejections used to repeat in the same magnetic configurations, which managed to restore their magnetic field and brightness in the lapse of time between the events.

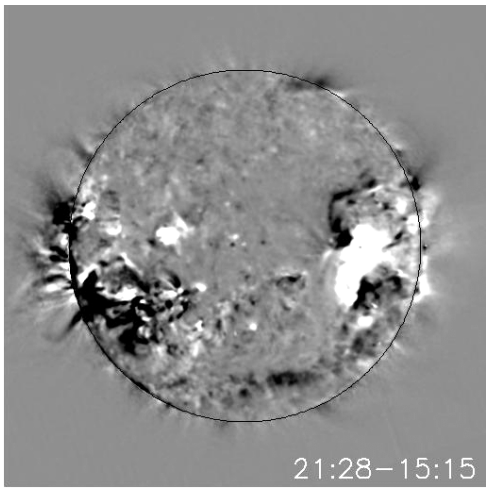

Fig. 11. Major solar flares and ejections observed on October 26, 2003 at wavelength of 175 Å

Observations with the RES-K Spectroheliograph in the resonance line MgXII (8.42 Å) allowed us to reveal and study a new class of the events in the solar corona – fast dynamic plasma features with temperatures up to 20 million deg., while the temperature of the solar corona itself was 1…2 million deg. It was the first time that images of these high-temperature features were obtained and their dynamics was studied. They are likely to form when the flare-generated hot plasma fills the magnetic configurations in the corona, and the plasma emission outlines various shapes (Fig. 12), such “hot clouds”, “spiders”, loops, propagating wave fronts, and successively glowing magnetic arcs. These events suggest a mechanism of the corona heating due to the release of magnetic energy in magnetic configurations and its transformation to the plasma energy. It is established that the hot plasma features in the corona are often accompanied by mass ejections from the solar atmosphere recorded with the coronograph on board the European mission SOHO.

For the first time, observations with the X-ray telescope operated in the coronograph regime provided data on the dynamics of the solar corona at a distance up to three solar radii. This region is important for understanding the origin of various phenomena. However, it is inaccessible to other instruments, being intermediate between the limb regions observed with telescopes and the far corona observed in the white light with coronographs. Here, one can readily isolate magnetic loops, arches, extended streamers, and solar-wind streams. The mass ejections and eruptive prominences were observed at these heights for the first time.

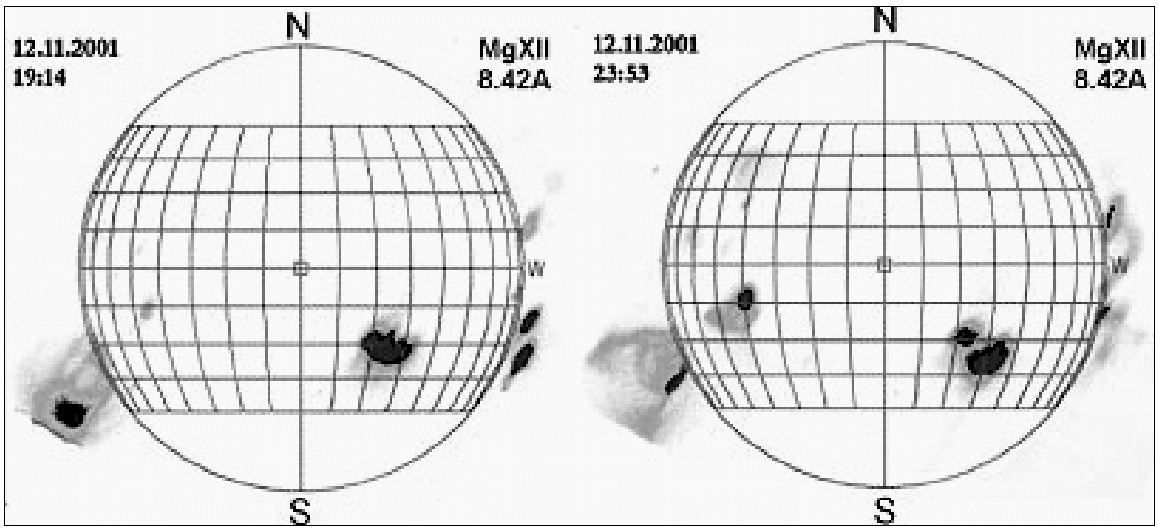

Fig. 12. Hot (up to 20 million deg.) plasma features in the solar corona as observed in the MgXII (8.42 Å) spectral line

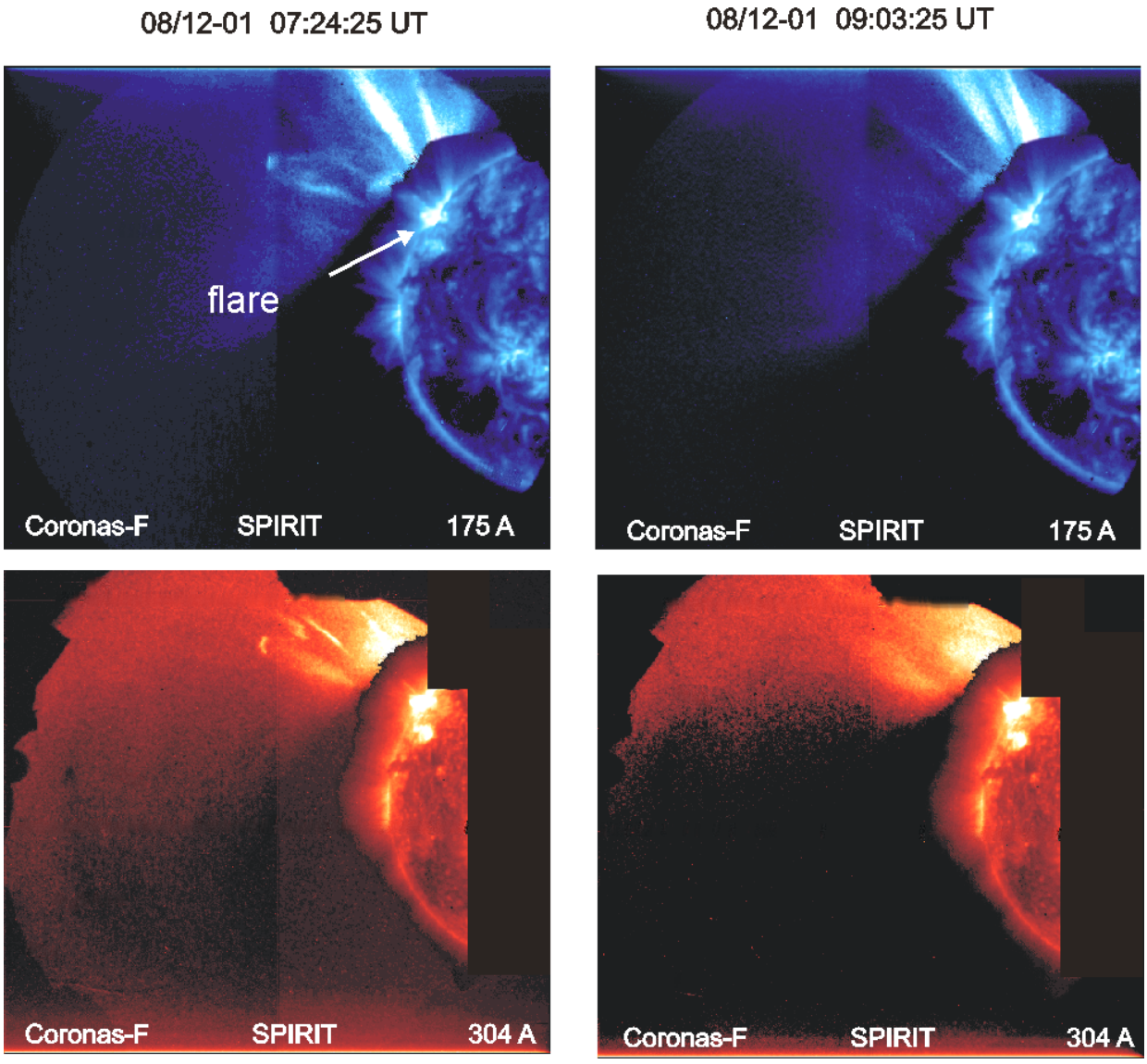

Fig. 13. Structure of the X-ray corona at a distance of three solar radii

Also for the first time, the X-ray coronograph provided the distribution maps of hard UV radiation in the quiet and disturbed corona with bright active regions on the limb. The maps illustrate the magnetic heating of the corona over the active regions.

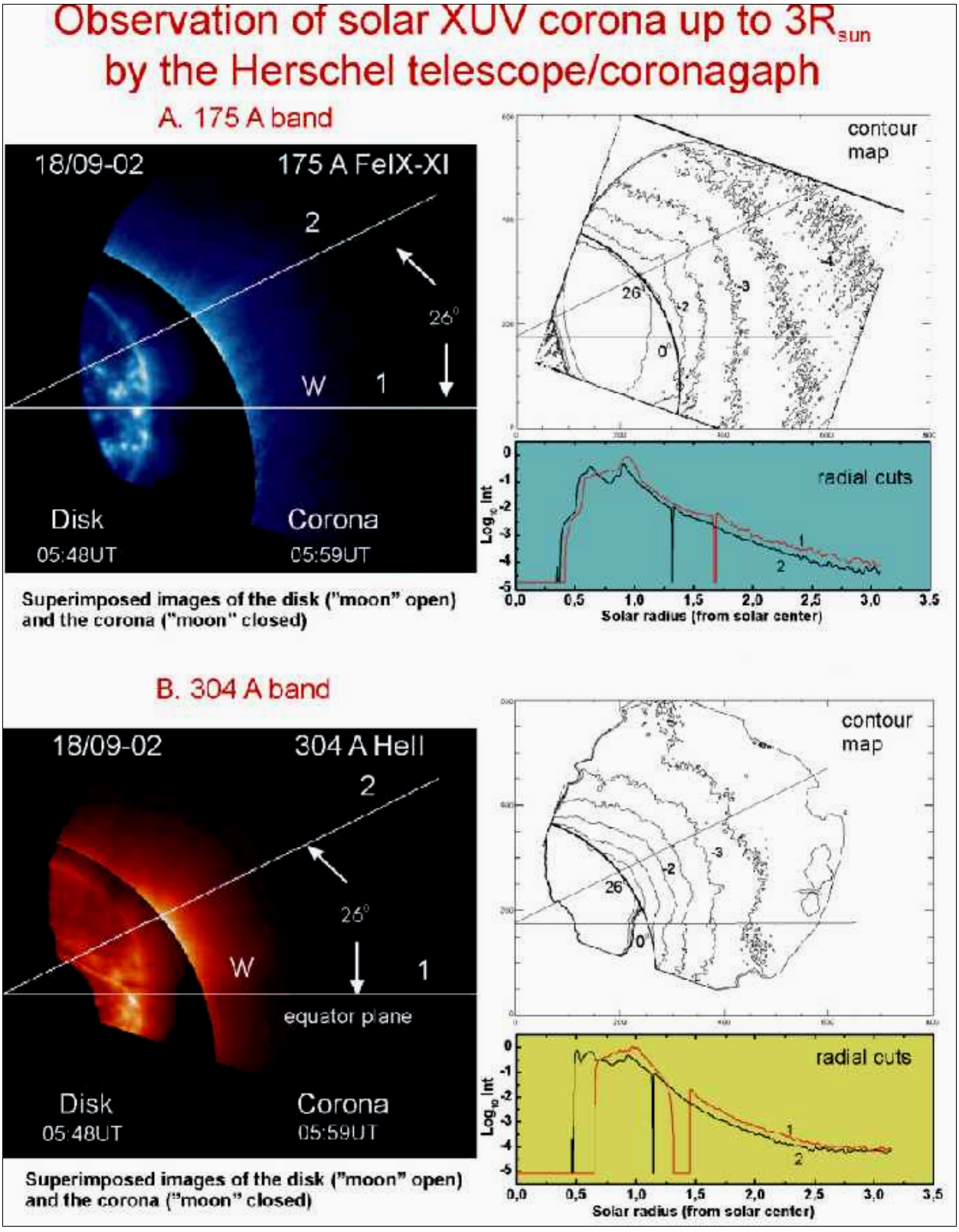

Fig. 14. Distribution of hard ultraviolet radiation in the quiet and disturbed corona with bright active regions on the limb

Events of September 2005.

The most interesting observation interval in 2005 (close to the minimum of the current cycle 23) was September 6–17, when a series of outstanding events occurred in the Sun, namely, 10 X-ray flares of importance X and 27 flares of importance M accompanied by powerful coronal mass ejections and strong geomagnetic storms. In that period, 13 flares were recorded by CORONAS-F/SPIRIT. The analysis of the coronal images obtained in the 175 Å lines with a temperature of about 1.2 MK shows that all flare events were accompanied by a dramatic reconstruction of the magnetic field lines in the flare region (see Fig. 15). A major limb flare of September 7, 2005 (the third in intensity during the current cycle) was accompanied by coronal mass ejections at a speed of about 550 km/s. As a result of these ejections, deep dimmings (temporary decreases of brightness associated with the mass evacuation during the ejection) appeared on the 175-Å solar images. On September 7, after the outstanding flare X17 at 17:40 UT and the associated coronal ejection, the decrease of the emission intensity at 175 Å in the dimming was about 7 % of the total solar irradiance. On September 13, after the flares X1.5 at 19:27 UT and X1.7 at 23:22 UT, the emission in the dimming decreased by about 5 %. Simultaneous observations of the solar corona with the CORONAS-F/SPIRIT spectroheliometer in the ranges of 177–210 Å and 280–335 Å provided the line spectra corresponding to the pre-flare and maximum phases of the flare evolution and allowed us to detect the appearance of multiple hot lines and the general increase of line intensities in the flare maximum phase. The intensity ratio of the emission lines in the spectra of the importance X17 limb flare recorded on September 7, 2005 were used to determine the differential emission measure. Its temperature dependence reveals that the peak of flare-generated plasma emission falls on the temperature range in the vicinity of 10 MK.

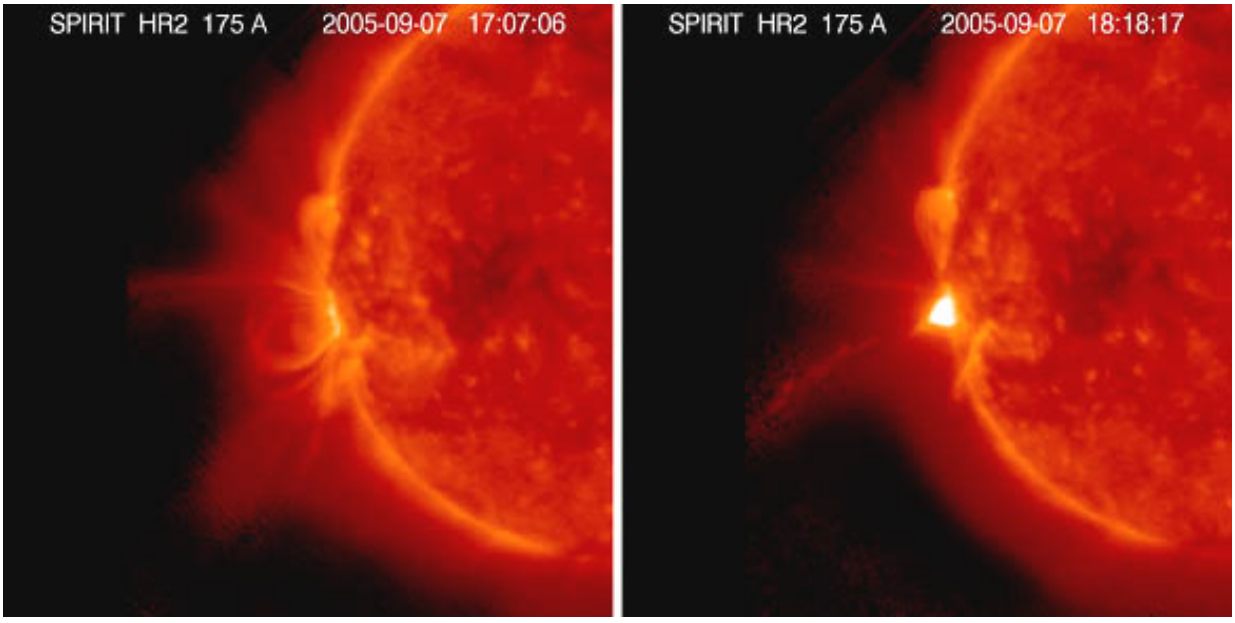

Fig. 15. Limb structure of the solar corona under pre-flare conditions (left) and in the maximum phase (right) of the importance X17 flare of September 7, 2005

Solar flares

"CORONAS-F" observations carried out with a high time and spectral resolution in a broad energy range (from optical to gamma radiation) provided a great body of new data on various physical processes in solar flares. These are spectral, energy, polarization, and dynamic characteristics of the flare-generated emission, spectra of accelerated particles, gamma lines, etc. (Fig. 16).

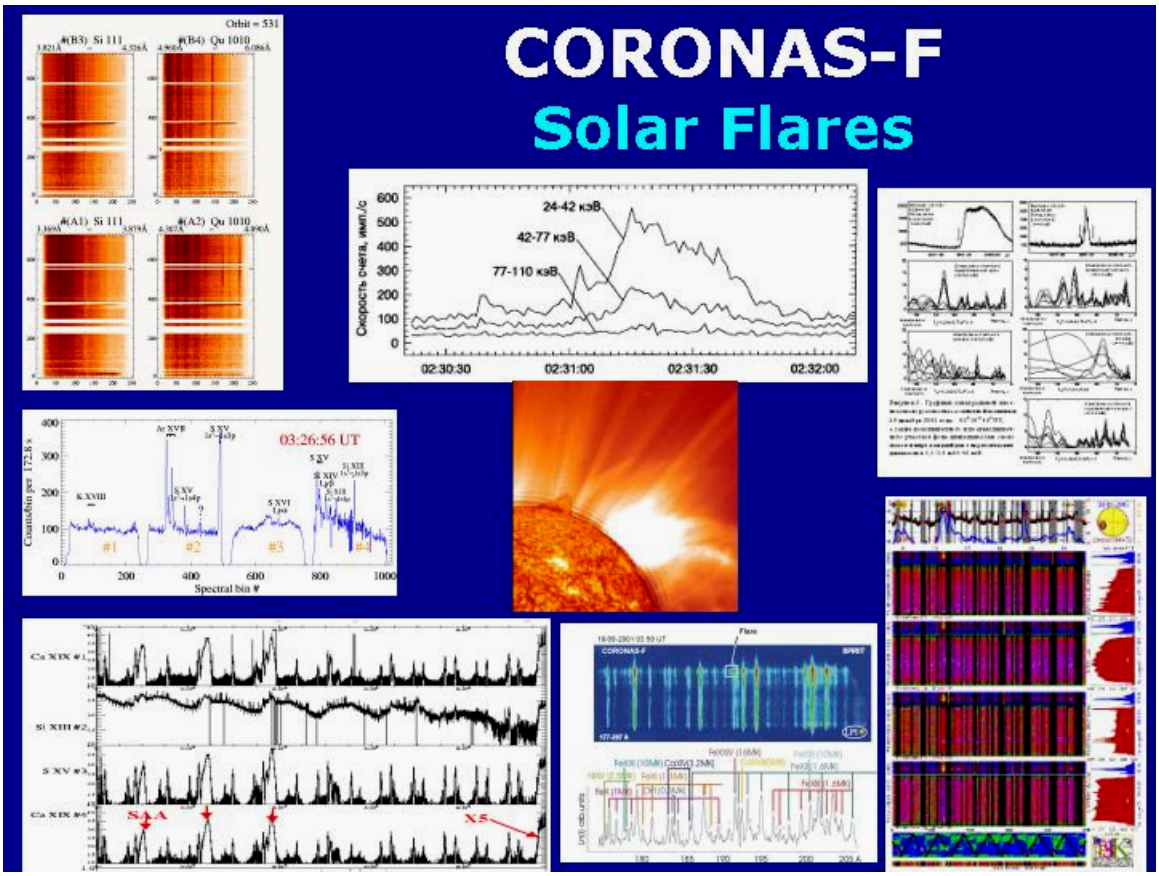

Fig. 16. Spectral, energy, and dynamic characteristics of flare emissions obtained with the "CORONAS-F" scientific complex

Magnetic heating of the corona

The high-sensitivity X-ray Spectrometer RPS-1 recorded pre-flare enhancements in the energy range of 3–30 keV and minor X-ray flares of importance C and M. Figure 17 illustrates the intensity time profiles and X-ray spectra of the importance M flare in different phases of its evolution: growth, maximum, and decay. The flare emission was the hardest at the peak of the flare evolution. Figure 18 shows the dependence of the X-ray background spectrum on solar activity in the absence of flares. The figure is based on the data for October 2003, when the solar activity level varied dramatically. The dependence in Fig. 18 illustrates the magnetic heating of the solar corona: the more sunspots are observed, the harder is the X-ray background spectrum. At the sunspot minimum, the spectrum is soft and is cut off at 6…7 keV. At the maximum, the spectrum becomes harder and reaches 20 keV due to the increased sunspot number and magnetic heating of the corona by active regions (AR484 and AR486).

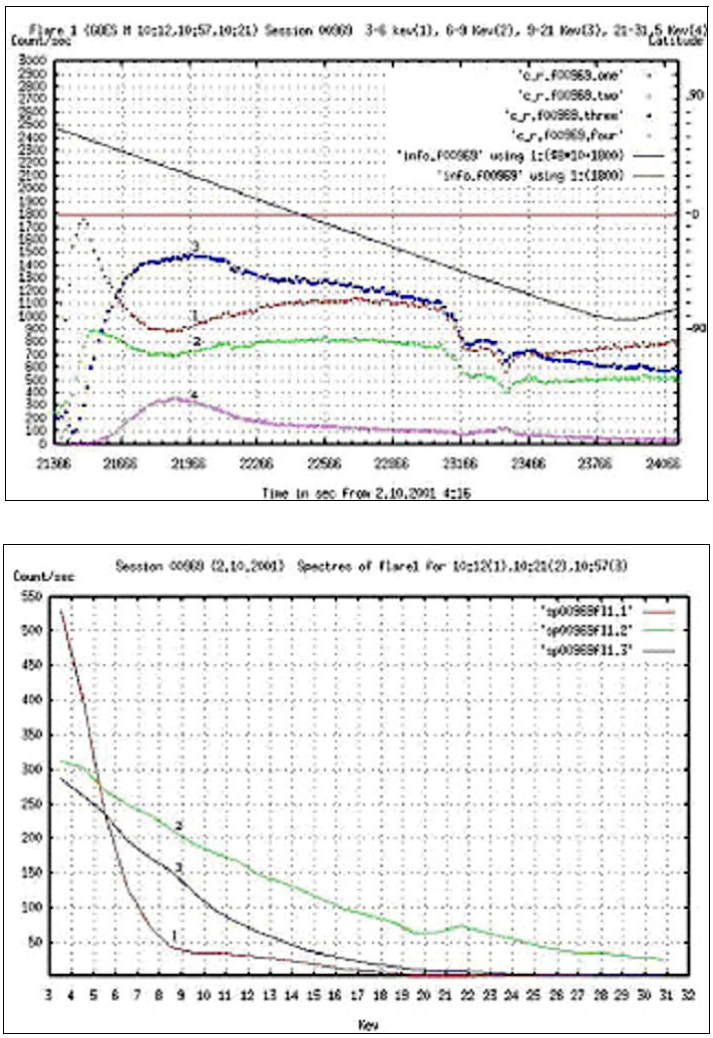

Fig. 17. Intensity time profiles and spectra of the importance M flare in different phases of the flare evolution: growth, maximum, and decay

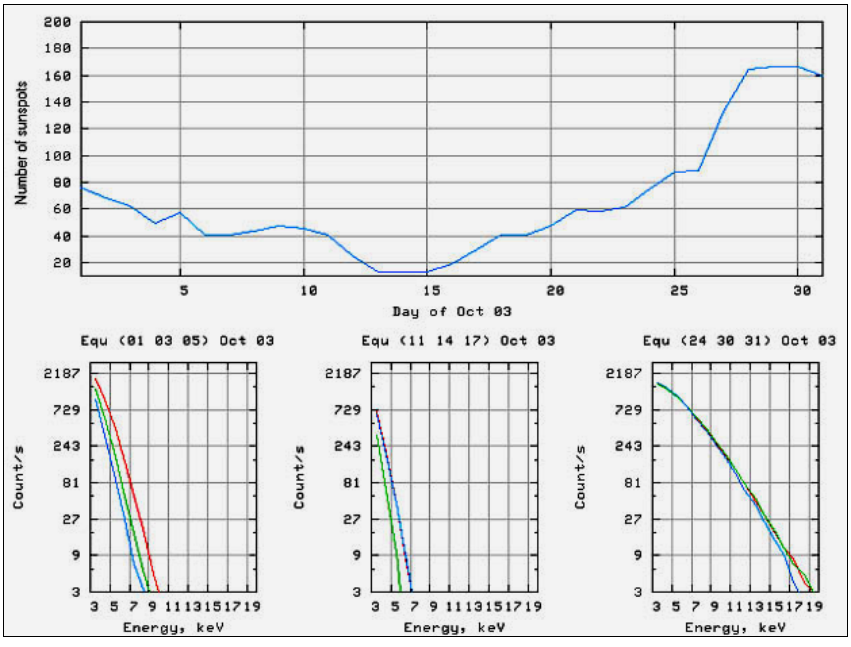

Fig. 18. X-ray background spectrum as a function of solar activity in the absence of flares illustrating the magnetic heating of the corona

Flare-generated X-ray emission

The mathematical treatment of the intensity time profiles of emission from minor flares obtained by Flare Spectrometer IRIS during 2005 and earlier revealed complex time features with the pulses of about 3–5 s in the profiles of soft and hard X-rays (3–40 keV), which could be isolated against the background of 10-s pulses. X-ray flux variations with a time scale of about 20 s were detected in the energy range of ~100–150 keV. The time structure of the emission intensity during the flare evolution was studied to reveal an intensive quasi-periodic component with a period of about 20 s and a few weaker components with the periods from 4 to 12 s existing in the pre-flare phase. In the post-flare phase, nearly all components split into two o more elements, and the emission energy is mostly concentrated in the region of small periods. The physical interpretation of these experimental data is associated with the complex magnetic features in the solar atmosphere (flare loops and arcades) treated as a system of interconnected oscillators, which can change their frequency and oscillation amplitude, collapse, and re-appear in the course of the flare evolution, as well as with the energy exchange between the flare loops. One-second oscillations of the emission intensity can be accounted for by MHD waves "running" along a magnetic loop as a result of disturbance at one end of the loop. For the typical parameters of the coronal plasma, the numerical estimates of the magnetic loop oscillation periods during a flare range from 2.2 to 66 s. The prognostic value of the results obtained is associated with early diagnostics of the flare evolution process on the basis of X-ray characteristics.

The dynamics of the hard X-ray energy spectra in different phases of the flare evolution followed with a time resolution of 1 s shows that, for some flares, the spectrum is perfectly well described in all phases by the power-law function with the power index changing in time. The spectrum index decreases at the peak of the emission intensity and increases in the decay phase. Flares were also observed, in which an intricately shaped spectrum consisting of two components was formed in the growth and maximum phases. The spectrum below 45 keV was, probably, formed by the thermal emission of hot plasma, and above 45 keV, by the bremsstrahlung of fast electrons. Such a shape of the spectrum was conserved in the flare decay phase. As the energy increased, the emission spectrum became steeper. This can be explained if we suggest that the distribution function of fast electrons responsible for the X-ray bremsstrahlung has a cut-off at a certain maximum energy of about 150–170 keV. The cut-off in the spectrum of fast electrons can arise due to interaction with plasma waves, taking into account the non-linear scatter of the latter on the background plasma ions.

Polarization of hard X-rays

The Solar Spectropolarimeter SPR-N measured for the first time the linear polarization of hard X-rays from a major flare (importance X-10) on October 29, 2003. In the impulsive phase, the polarization reached a significant value (Fig. 19). This is the first direct evidence that the accelerated particle beams do not only exist

but are rather accelerated by pulsed electric fields than some stochastic mechanism.

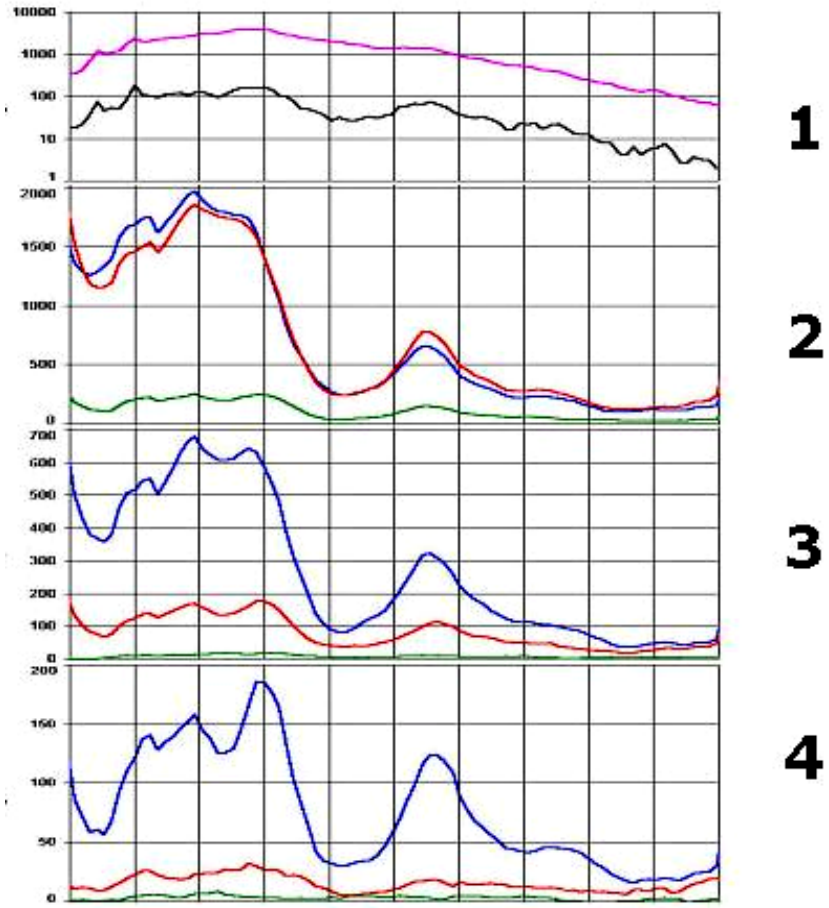

Fig. 19. Difference in the readings (number of pulses per 4 s) of three polarization detectors of the SPR-N device (curves of different colors) illustrating the linear polarization of hard X-rays at the flare maximum on October 29, 2003: energy ranges of 20–40 keV (panel 2), 40–60 keV (panel 3), and 60–100 keV (panel 4). Panel 1 represents the readings of the patrol detector (photons/cm^2·s) in the energy ranges of 15–40 keV and 40–100 keV

Atomic processes in flares

The measurements with the X-ray Spectrometer RESIK and Spectrophotometer DIOGENESS allowed a detailed spectroscopic diagnostics of the flare-generated plasma and atomic processes in flares. For the first time, the RESIK Spectrometer observed strong spectral satellite lines of transitions of the type $1s^2$–$1snp$, $n = 3, 4, 5$ for the sulphur (S) and silicon (Si) ions and spectral lines of ions of astrophysical plasmas corresponding to transitions 1s–np and $1s^2$–$1snp$ for the quantum number $n \sim 4$–9 (Fig. 20). The use of the intensity ratio of these spectal lines provides us with a new method of temperatue diagnostics of the coronal plasma. Owing to its high sensitivity, the X-ray spectrometer RESIK can measure the line-to-continuum intensity ratio depending on the elementary constitution. These data allowed us to determine for the first time the absolute content of potassium (K) and chlorine (Cl) in the solar corona (Fig. 21), to measure a few thousand spectra of various elements and ions of solar plasma in the

previously unexplored spectral range, to detect new spectral lines, and identify some of them (Fig. 22). By way of example, we can mention the observed lines of the highly ionized chlorine (Cl XVI) in the range of 4.4–4.5 Å. About one million line spectra were obtained for the period from August 2001 to May 2003. Numerous observations (more than 1200 time intervals at different level of solar activity) have been analyzed to study the temperature dependence of the solar plasma ion spectra (the shape and intensity of the spectral lines). A catalog of the RESIK data is available on the Internet site (http://www.cbk.pan.wroc.pl/resik_catalogue.htm). An atlas of the solar spectral lines in the range of 3.4–6.1 Å was compiled on the basis of these data. The absolute Doppler shifts of the X-ray spectral lines during the flare growth phase (flare X5.3 25 25 of August 2001) were determined for the first time using the DIOGENESS spectrophotometer data. A few hundred spectra of the helium-like ions Ca XIX, S XV, and Si XIII were measured, and about 2500 X-ray line spectra were obtained for the flares observed during August and September 2001.

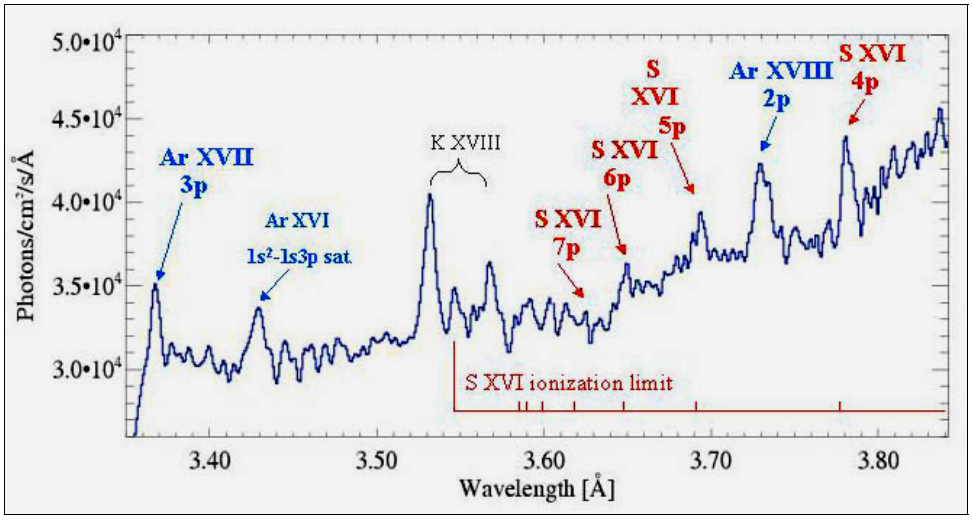

(a)

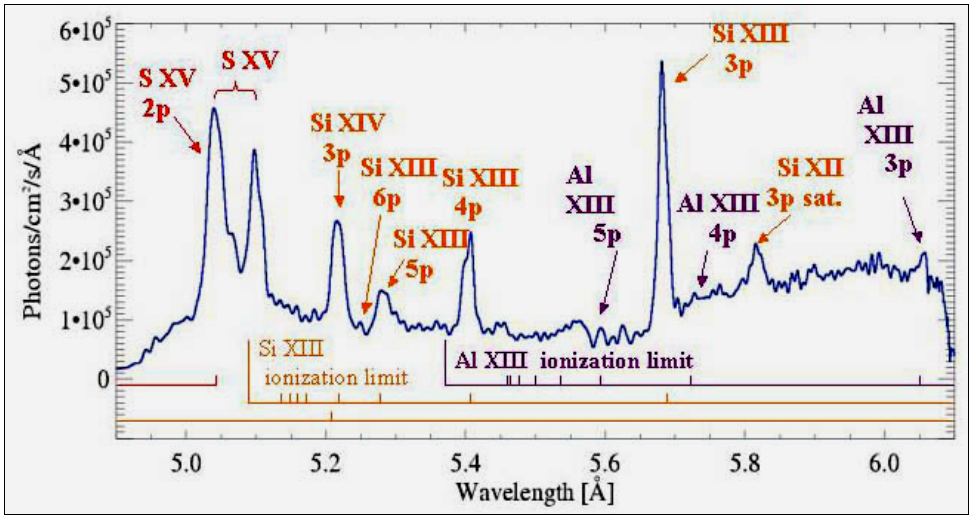

(b)

Fig. 20. Strong spectral satellite lines of S XV and other ions ((a) and (b)) and the lines of helium-like ions SiXIV and AlXIII (b), corresponding to the atomic transitions with a high quantum number n: from $n = 3$ up to the ionization limit

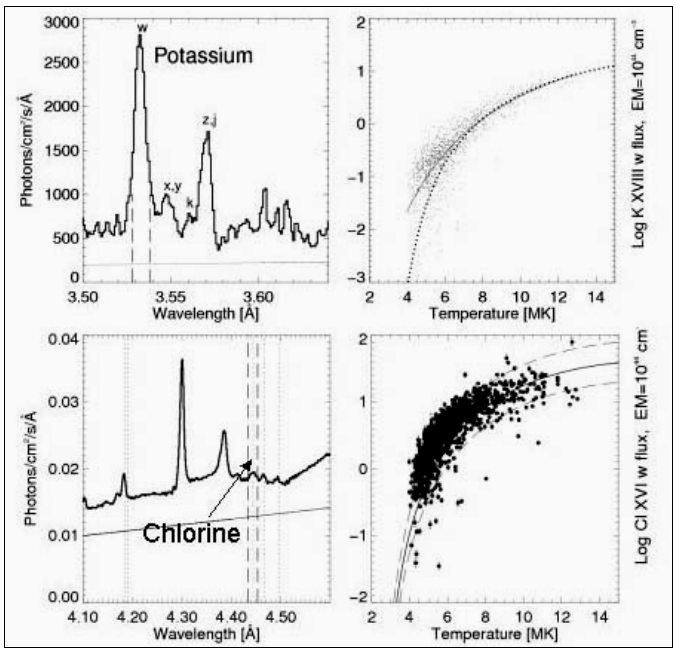

Fig. 21. Absolute content of potassium (K) and chlorine (Cl) in the solar atmosphere as inferred from the intensity ratio of line emissions in the continuum

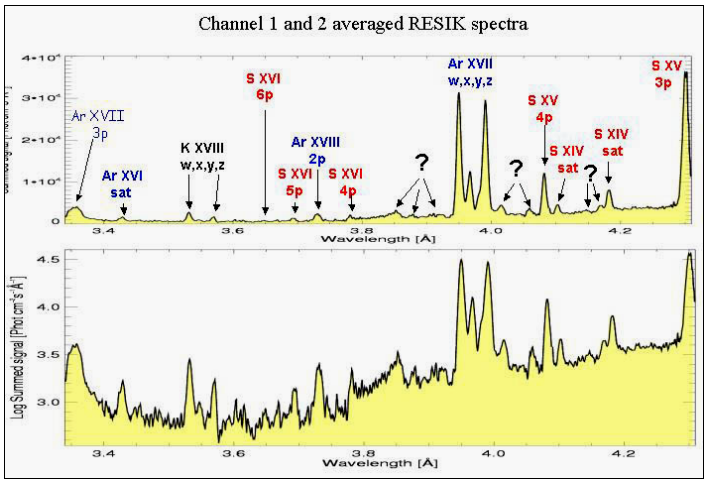

(a)

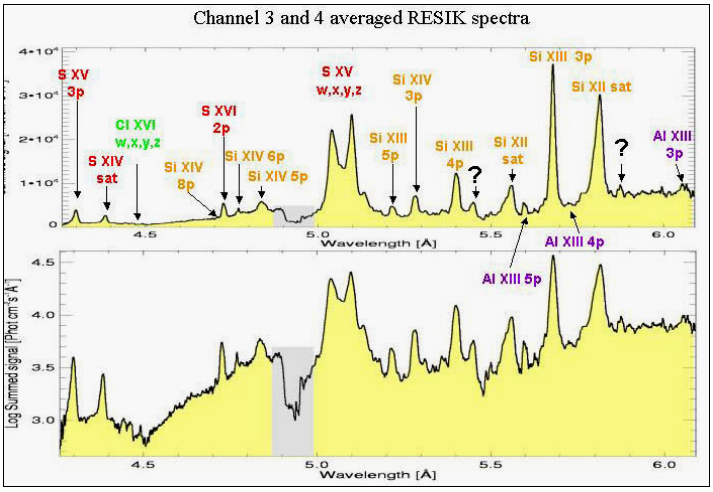

(b)

Fig. 22. Spectral lines of the flare-generated plasma: (a) in the RESIK spectral channel 3,3–4,3 Å and (b) in the channel 4,3–6,1 Å

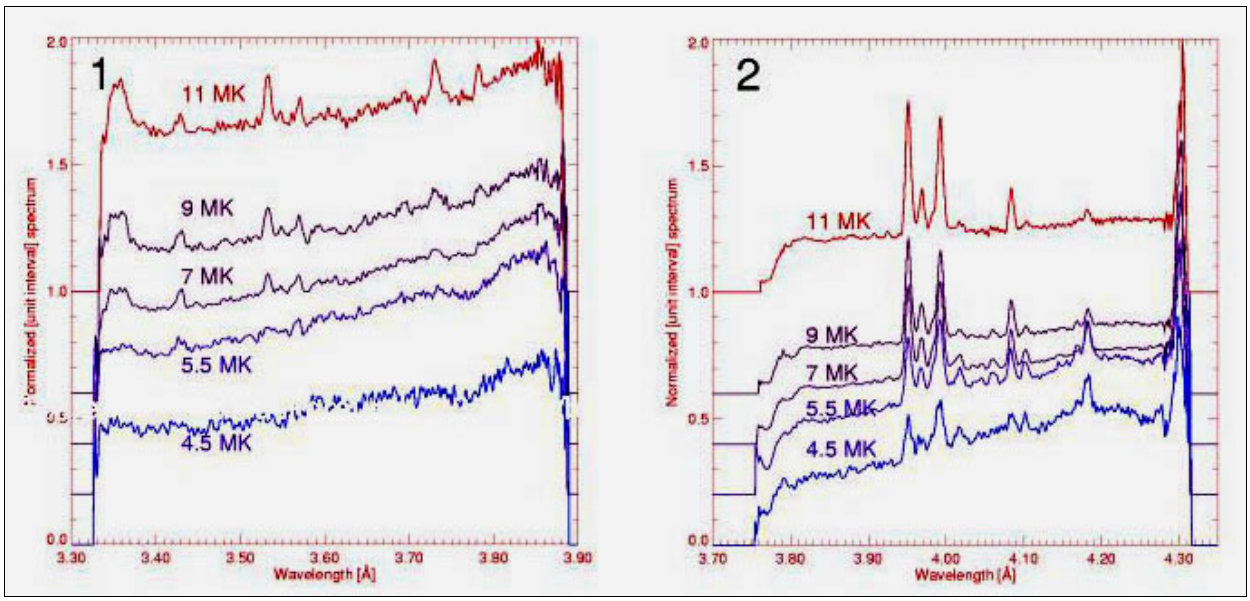

Fig. 23. Emission spectra of the solar plasma ions as a function of plasma temperature

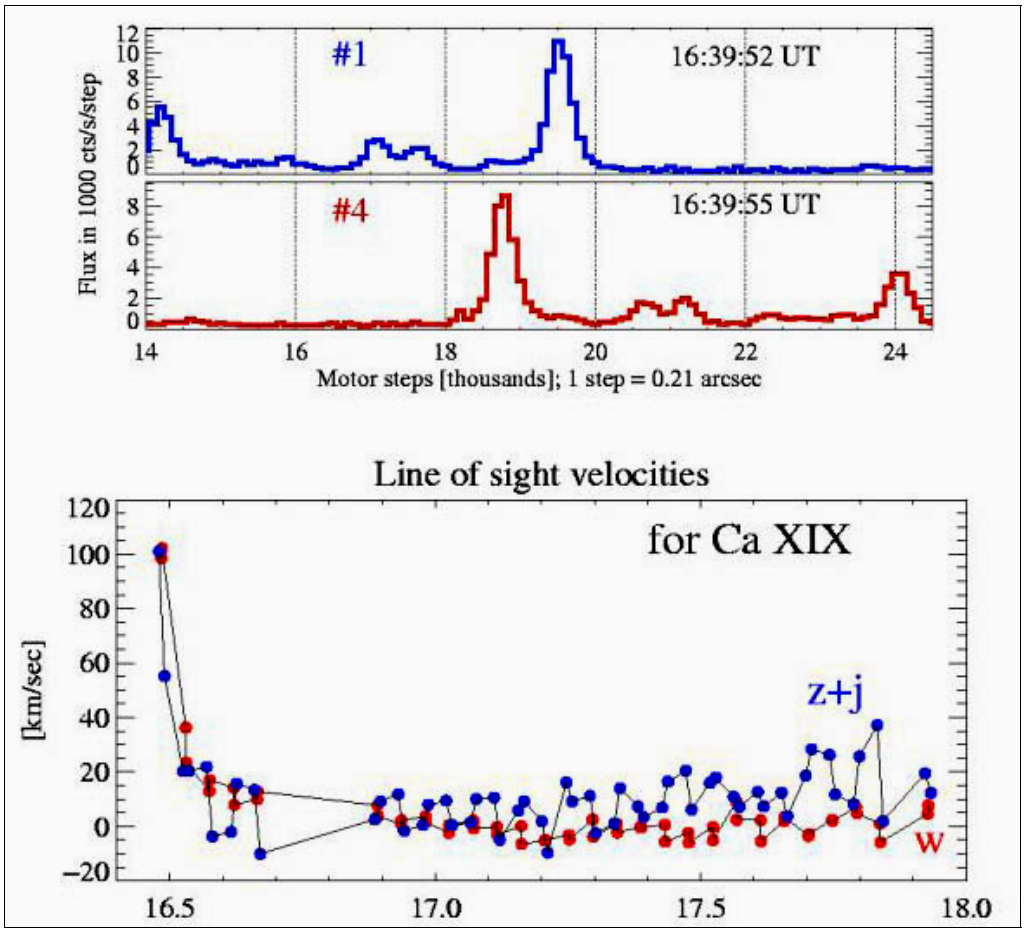

Fig. 24. Absolute Doppler shifts of X-ray lines and velocities of hot flare plasma at the early stage of the X5.3 flare of August 25, 2001

The emission spectra from solar flares obtained with the RESIK device were analyzed by different methods and allowed us to determine thermodynamic characteristics of the emitting plasma, such as temperature (T), emission measure

(EM), and temperature distribution of the differential emission measure (DEM), and to study their time variations. Figure 25 illustrates the time variation of temperature calculated under one-temperature approximation from the observed and theoretical spectra (upper curve) and the so-called thermodynamic measure $ThM = T(EM)^{1/2}$ (characterizing the quantity of the plasma thermal energy in the emitting volume). The maximum temperature is observed 10 min. before the maximum thermal energy. The temperature distribution of the differential emission measure (DEM) characterizing the quantity of plasma in the particular temperature ranges is shown in Fig. 26 for two flares. For the flare of importance M1.9 on January 21, 2003 (left), besides the growth (15:00 UT), maximum (15:15 UT), and decay phases (16:30 UT), the figure represents the DEM curve corresponding to the late decay of the flare (18:15 UT). In general, the distributions observed during 3 hours comprised two components: cold plasma with a temperature of 5–8 MK and hot plasma with a temperature of 18–25 MK. The temperature of cold plasma remained almost invariable during the flare, though its quantity changed essentially. In the late decay phase, the quantity of cold plasma was nearly an order of magnitude smaller than in the growth phase. The quantity of hot plasma decreased in the decay phase much stronger (by two orders), and its maximum temperature changed from 22 MK at the peak of the flare evolution to 20 MK three hours later. In the short-lasting (12 min) X-ray flare of importance C5.8 recorded on February 22, 2003 (right-hand part of Fig. 26), the plasma was mostly concentrated in two temperature components. In this case, however, the cooling of hot plasma from 22 MK in the growth phase to 19 MK in the decay phase took a few (six) minutes. The quantity of hot plasma in the decay phase was an order of magnitude smaller than at the maximum.

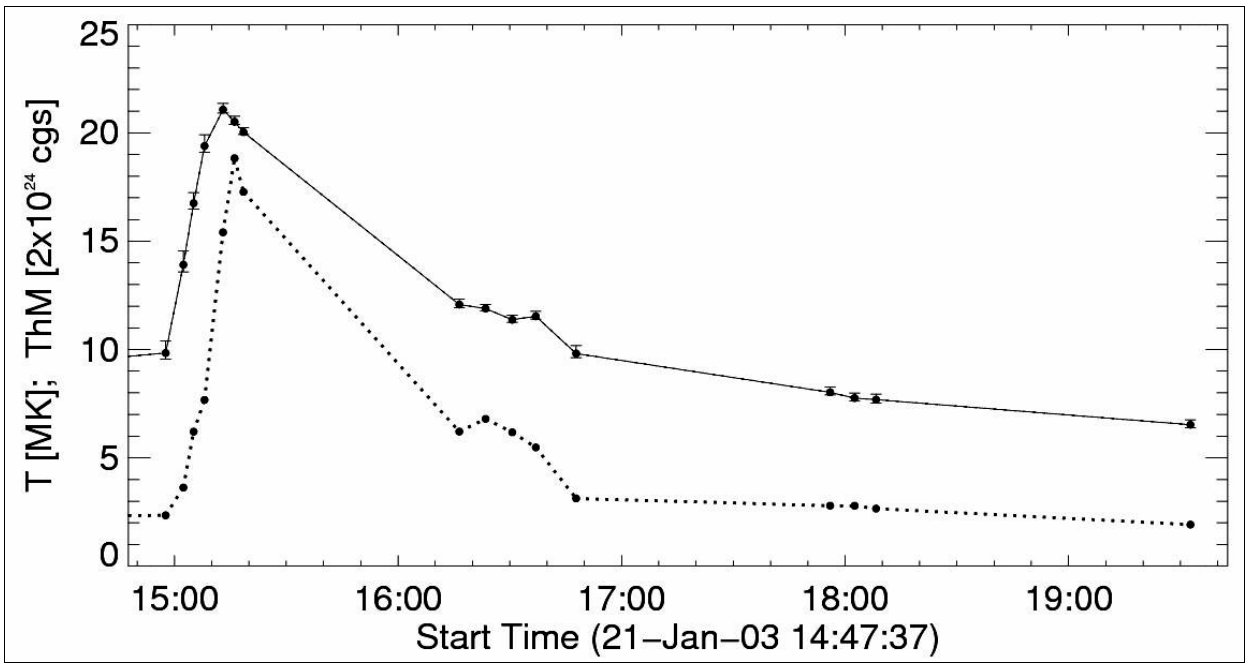

Fig. 25. Time variations of the temperature (upper curve) and thermodynamic measure (lower curve) for the flare of January 21, 2003. The scales of the curves are shifted so that the curves do not intersect

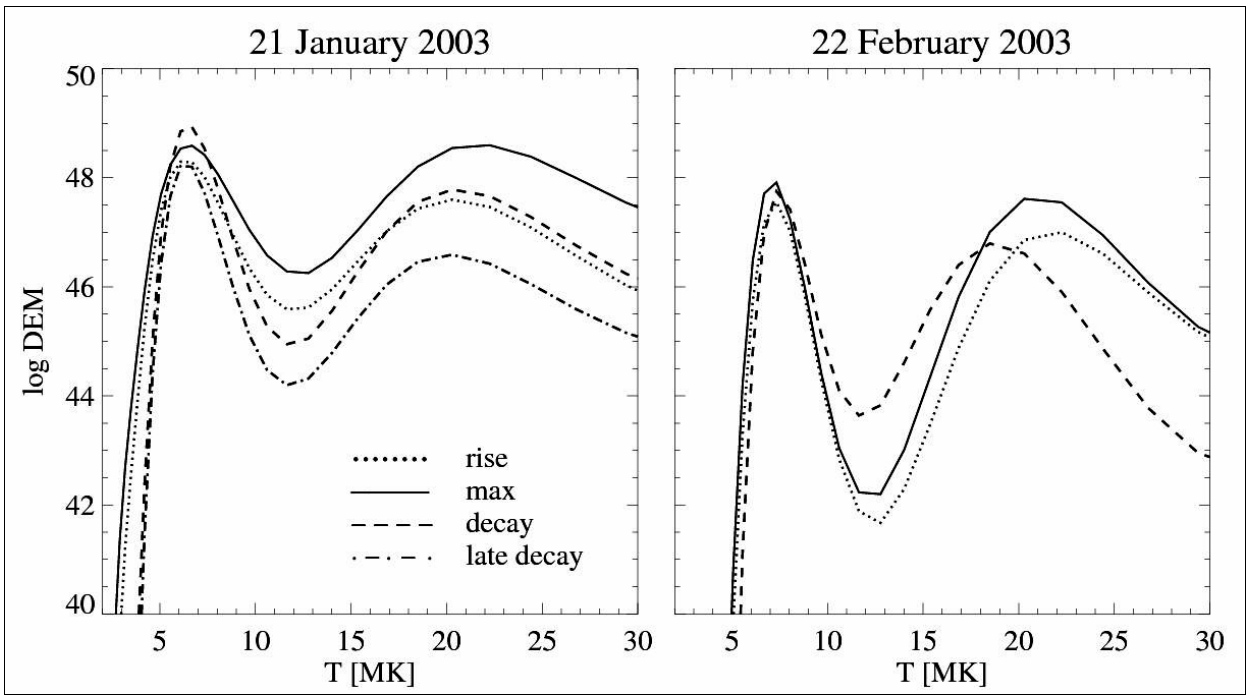

Fig. 26. Temperature distribution of the differential emission measure for two flares: the long-lived limb X-ray flare of importance M1.9 (January 21, 2003) and the short-lived flare of importance C5.8 observed on the disk on February 22, 2003

Nuclear processes in flares

"CORONAS-F" observations of gamma-rays generated in collisions of the flare-accelerated particles with nuclei provided us with rich diagnostic information on the acceleration process in flares and composition of the solar atmosphere.

Figure 27 provides an example of gamma-lines recorded with the Amplitude-Time Spectrometer AVS during the flare of October 29, 2003. The record reveals various chemical elements and their isotopes present in the solar atmosphere, namely, iron, magnesium, silicon, neon, oxygen, and carbon. One can also see a spectral feature corresponding to the nuclear line of the trapped flare-generated neutrons. Since the gamma radiation generated in a flare consists of the emission of individual gamma-lines excited by the accelerated protons, the gamma spectrum under consideration characterizes simultaneously the primary spectrum of the flare-accelerated protons, which is one of the most important characteristics of the acceleration process.

The time profiles of the counting rates of gamma quanta from a number of solar flares obtained with the AVS device in various energy ranges corresponding to the nuclear lines, positron line, and neutron trapping line were analyzed to reveal features with the time scales from 16 to 80 s. A similar analysis in the energy range of 0.1–20 MeV with a time resolution of 1 ms showed the presence of fine structures with the typical time scales from 7 to 35 mc in the time profiles of some flares (e.g., in the flare of January 20, 2005).

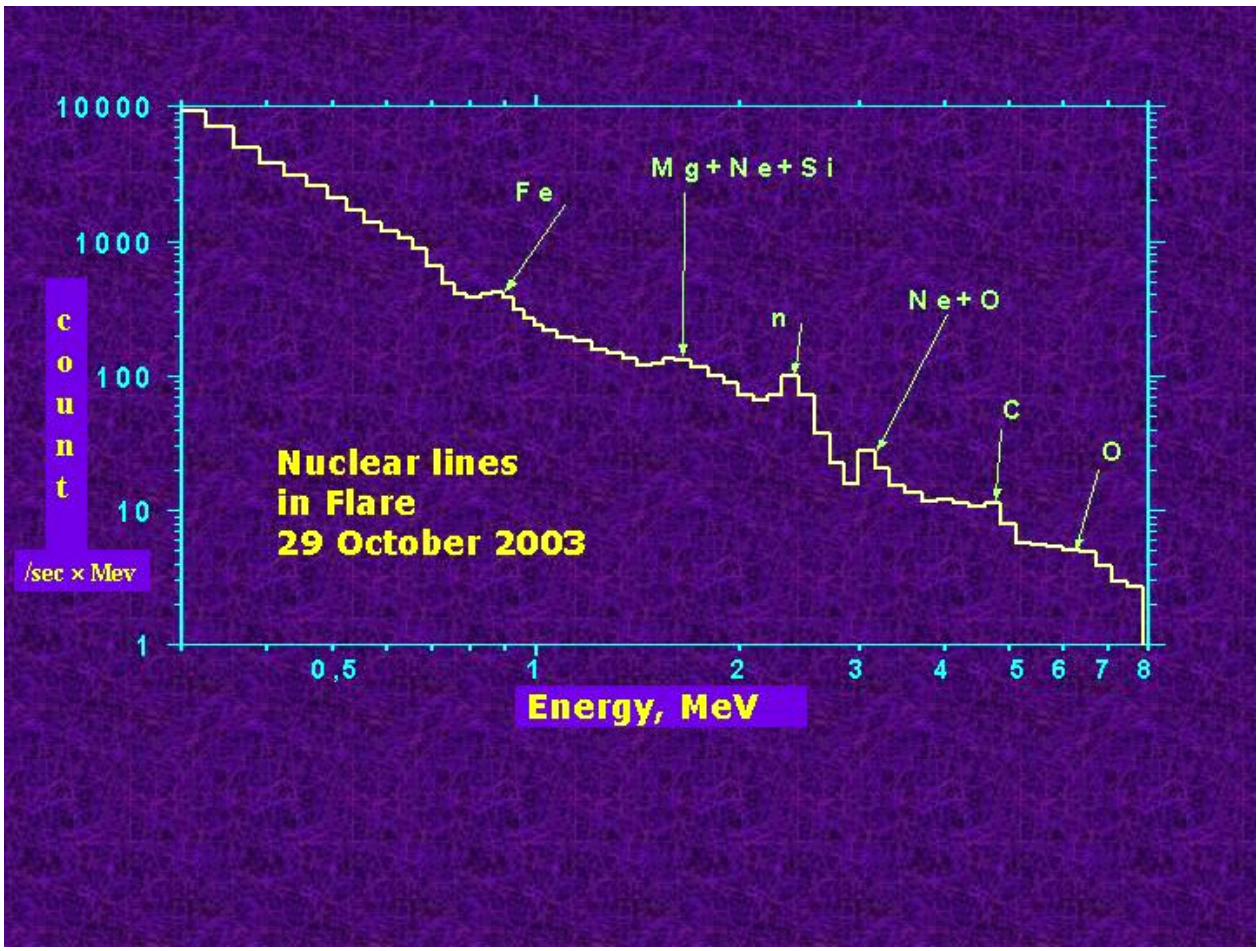

Fig. 27. Gamma-lines from the flare of October 29, 2003 indicating the presence of various chemical elements and their isotopes in the solar atmosphere

The neutrons generated in solar flares can be detected at the Earth's orbit only if their energy exceeds 30 MeV. At lower energies, they decay to a proton, electron, and electron anti-neutrino (beta decay of neutrons; the decay time in the vacuum is 16 min) before reaching the Earth. Unlike the protons and electrons accelerated by pulsed electric fields in flares, the high-energy neutrons can only form in nuclear reactions in the course of interaction of accelerated protons with the nucleons (or nuclei) of solar plasma. Since the neutrons have no charge and are not affected by the magnetic field, they move from their origin to the detector along straight lines contrary to the protons and electrons, which move along the magnetic field lines so that, at the same energies and velocities, it takes them longer to reach the Earth's orbit. Hence, there must be a delay between the arrival of neutrons and protons generated simultaneously in solar flares. Figure 28 illustrates the gamma and neutron fluxes recorded with the SONG Spectrometer of solar neutrons and gamma-radiation during the major flares of October and November 2003. These data compared with other observations allow us to determine the escape time of the accelerated protons and high-energy neutrons from the solar corona.

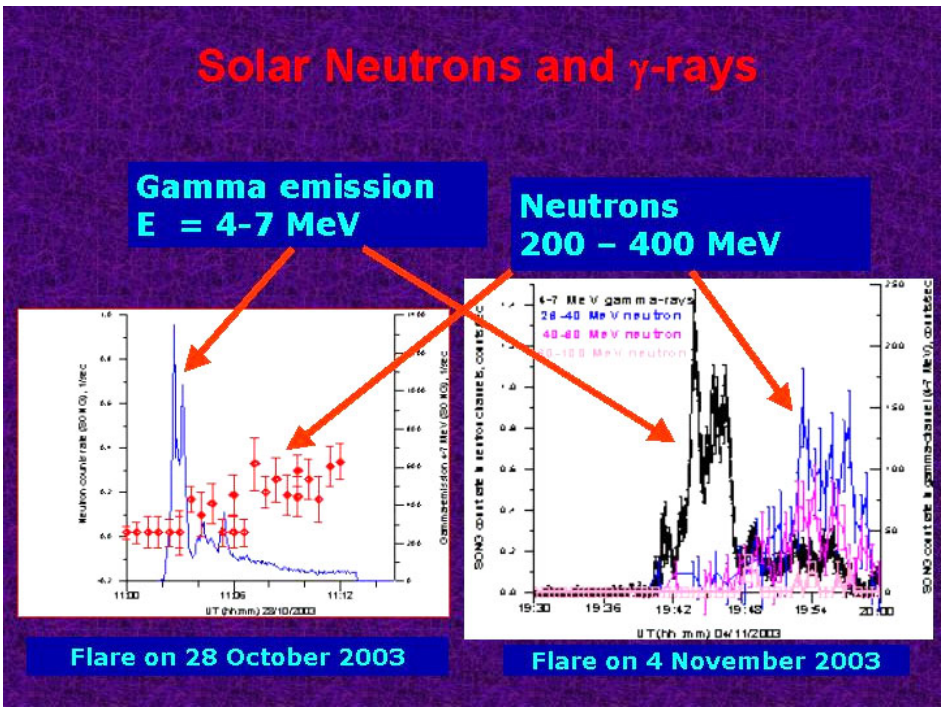

Fig. 28. Gamma-ray and neutron fluxes from the solar flares of October 28 and November 4, 2003

Ultraviolet emission of solar flares

The Solar Ultraviolet Radiometer SUFR and Ultraviolet Spectrophotometer WUSS were used to measure the ultraviolet (UV) emission fluxes from solar flares. Figure 29 shows an example of such measurements in the Lα line (at wavelengths shorter than 130 nm) taken with the WUSS device during the flare of 21.01.2003. The typical variation of ultraviolet emission in the Lα wavelength range for the X-ray flares of importance C9-M1 is about 5 %. In the most intensive flares, the increase of ultraviolet emission in the 120-nm band does not exceed a few percent.

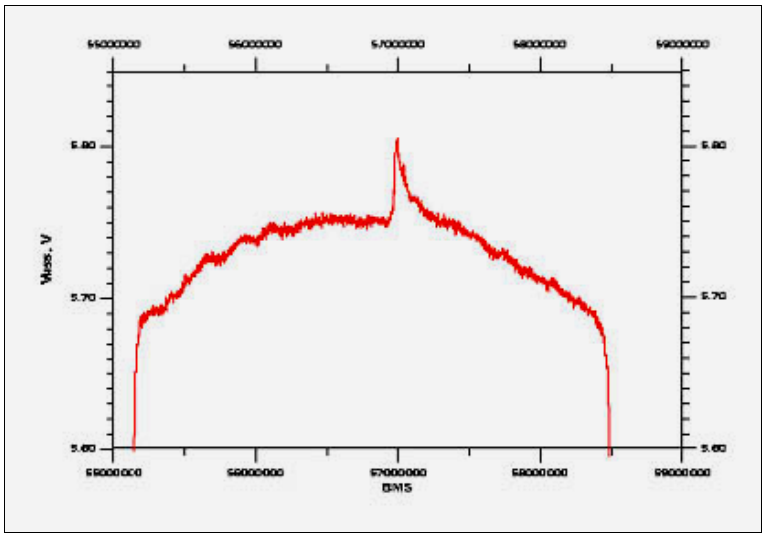

Fig. 29. UV flux from the solar flare of January 21, 2003 in the Lα line (wavelengths shorter than 130 nm)

Solar cosmic-ray measurements in near-Earth space

The "CORONAS-F" SCR complex designed for measuring solar cosmic rays along the satellite orbit provided a continuous series of data on solar energetic particle fluxes. The data on electron fluxes with the energies above 300 keV are unique, since no other such measurements exist at present. The SCR measurements obtained allow us to study the dynamics of the Earth's radiation belts and penetration of high-energy solar particles to the magnetosphere during strong geomagnetic storms, including not only the inner and outer radiation belts, but also the intermediate region.

The events of October and November 2003, when major flares in the Sun caused two severe magnetic storms, were analyzed to study the deformation of the magnetosphere and radiation belts, namely, the motion of the radiation belts inside the magnetosphere accompanied by penetration of the solar energetic particles (Fig. 30). In the course of this study, we found a new effect consisting in disappearance of the outer radiation belt of electrons in the main phase of the magnetic storm at energies higher than 1.5 MeV. This is likely to be due to the electron precipitation into the loss cone during geomagnetic disturbances.

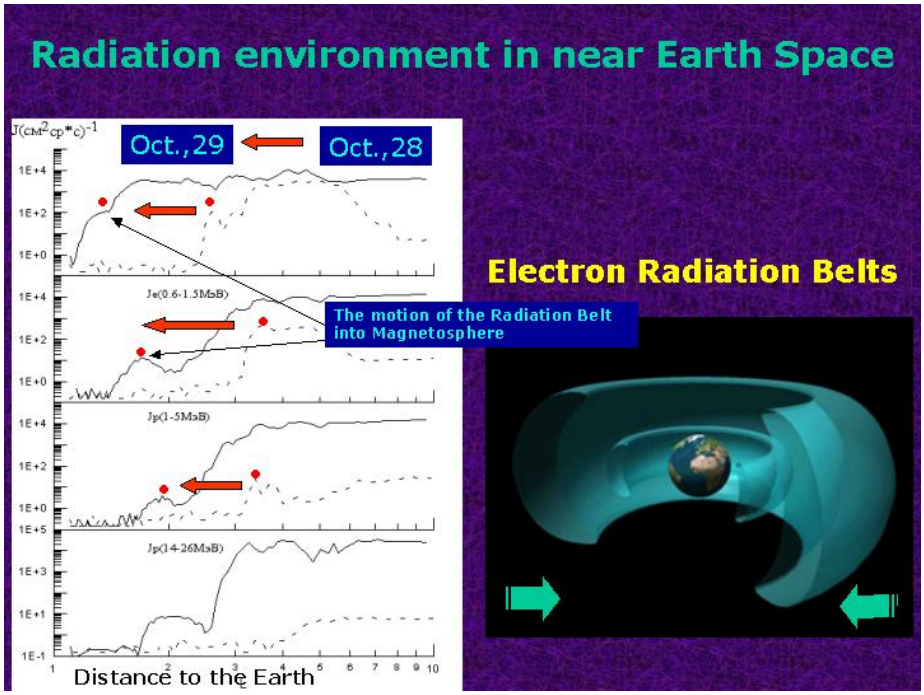

Fig. 30. Motion of the radiation belts inside the magnetosphere accompanied by penetration of solar energetic particles during the solar event of November 28–29, 2003

Among the records of solar cosmic rays with the "CORONAS-F" SCR complex and the magnetospheric response to solar flares and ejections, we can isolate an interesting interval of January 15–21, 2005. In that interval, several flares occurred producing large fluxes of energetic particles and a coronal mass ejection, which caused strong disturbances in the magnetosphere and radiation belts. The most complete data are available for the flare of January 20, 2005 (Fig. 31), which was recorded when the satellite was crossing the equator. During

the decrease of the high-energy gamma-quanta against the GCR background, we measured an additional increase of the high-energy particle flux (Fig.31, lower panel) and, using the latitudinal geomagnetic cut-off (i.e., at the anomaly of the GCR latitudinal variation), estimated the energy of the first particle arrival (~5 GeV).

An enhancement of the high-energy particle flux was recorded at the L-shell of ~1.5 at 6:56 UT, while the neutron monitor readings at the South Pole station began to increase at 6:49 UT. The delay in recording the flare-accelerated protons with the threshold energy of 6 GeV at L ~ 1.5 suggests that this is the maximum energy for these particles. A preliminary analysis of the SPR-N and SONG data from the "CORONAS-F" and GOES satellites shows that the energy release of the flare under discussion was mainly in the form of accelerated particles. The flare-generated coronal mass ejection reached the Earth's magnetosphere on January 21, and the magnetospheric disturbance developed mainly at the positive IMF Bz component. The dayside magnetopause approached the Earth to the distance of $5R_E$, and the outer boundary of the radiation belt moved to the shell L ~ 3. The relaxation of the radiation belt after the storm lasted longer than it does in the case of the classical storms.

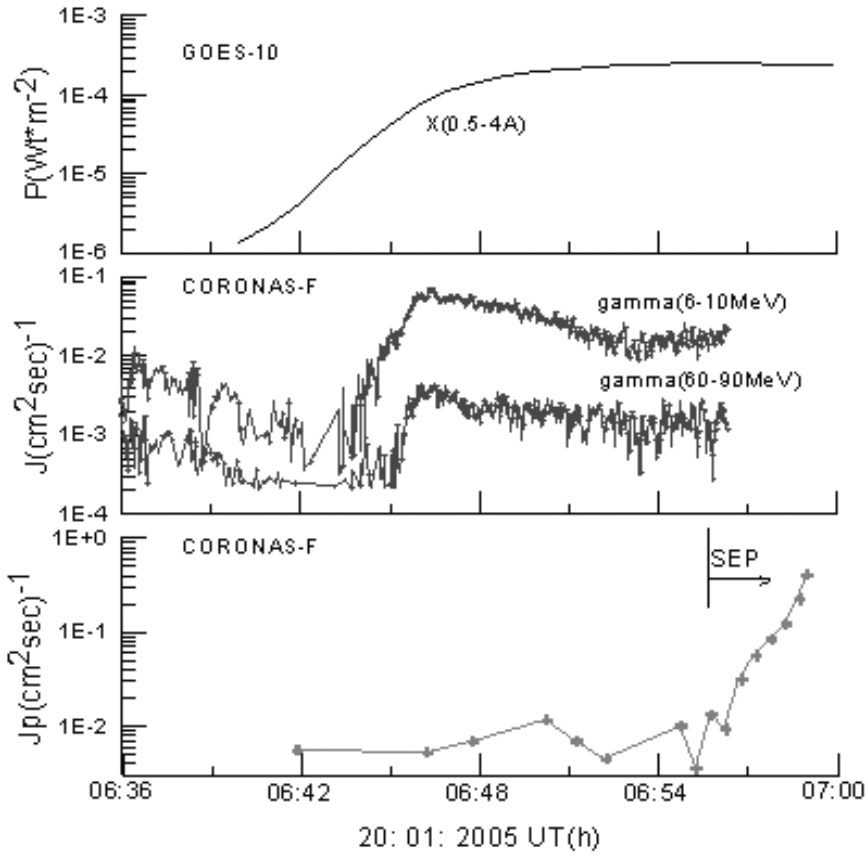

Fig. 31. Flare emission of January 20, 2005. Thermal X-ray flux in the range of 3–24 keV (GOES-10) (top); counting rates of the hard gamma quanta from the bremsstrahlung in the range of 6–10 MeV and from the decay of pions generated in nuclear reactions of the accelerated relativistic protons with nuclei in the solar corona in the range of 40–90 MeV (middle); and additional increase of the counting rate of energetic charged particles (protons) in the energy range > 100 MeV (bottom). SEP — solar energetic particles

Along with the well-known precipitations of energetic particles from the magnetosphere into the ionosphere in the Polar Regions and in the Brazil anomaly zone, the AVS device detected localized (about 30° geographical latitude and 10° geographical longitude) quasi-stationary low-latitude and equatorial precipitations (Fig. 32). The origin of these phenomena is not clear. They are characterized by a noticeable increase of the radiation background (by 20–30 %), and their lifetime may reach 8 days.

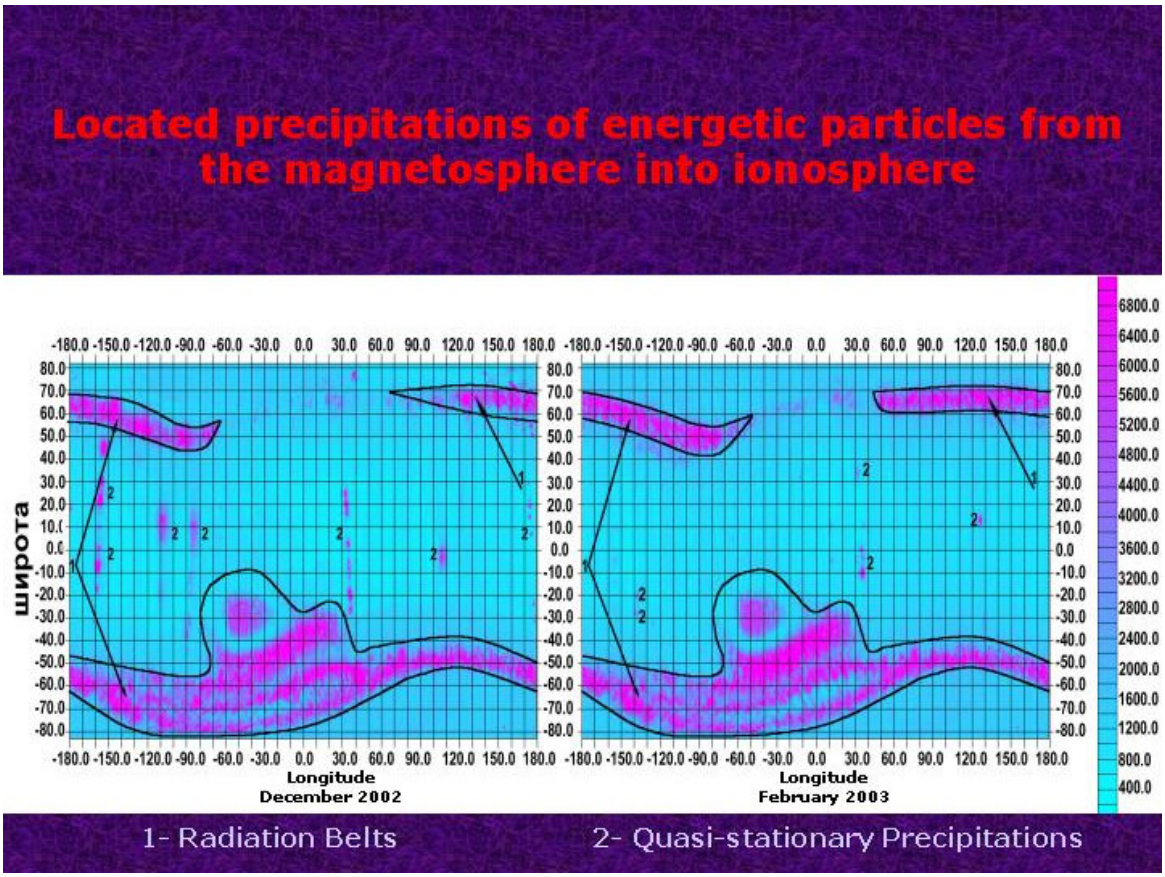

Fig. 32. Maps of quasi-stationary precipitations of energetic particles from the magnetosphere into the ionosphere: 1 — radiation belts, 2 — quasi-stationary precipitations

Study of the Earth's upper atmosphere

The solar X-ray Telescope on board the CORONAS-F mission was used to study the Earth's upper atmosphere by the absorption of the solar hard X-rays as the satellite entered and left the Earth's shadow (Fig. 33). The data obtained allow us to determine the height dependence of the X-ray absorption coefficient with a resolution increased 100 times (Fig. 34). We studied the density and composition of the Earth's atmosphere at the height of 500 km and their dependence on the solar activity level and determined the content of the molecular nitrogen and atomic oxygen. For similar observations in the UV range with the SUFR Radiometer and WUSS Spectrophotometer, a method was developed for determining the content of the molecular oxygen — one of the basic atmospheric constituents. The observations under discussion provided us with the experimental data necessary for updating the model of the Earth's atmosphere.

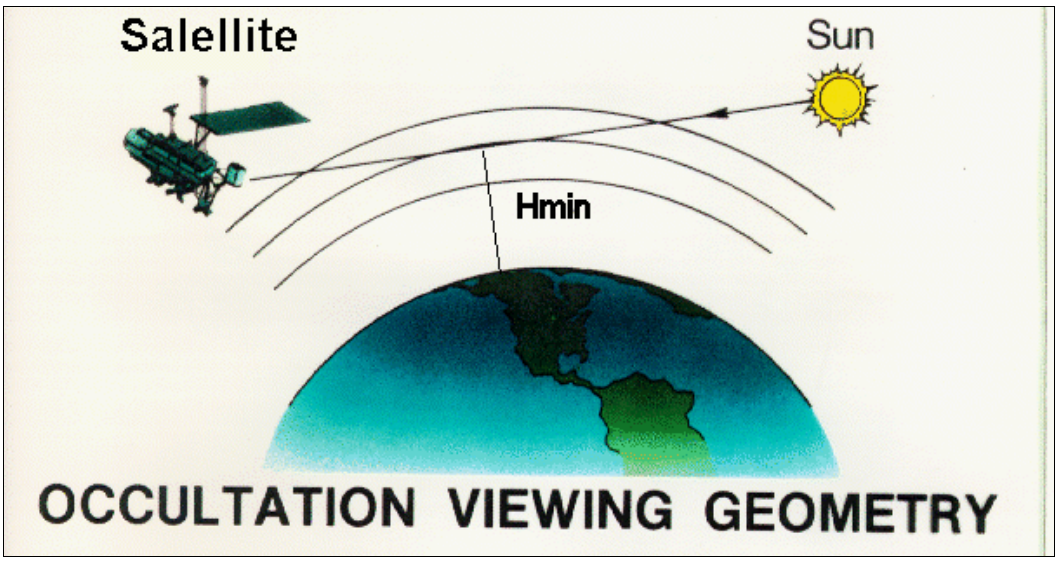

Fig. 33. The scheme for measuring the transparency of the Earth's atmosphere based on observations with the CORONAS-F X-ray telescope

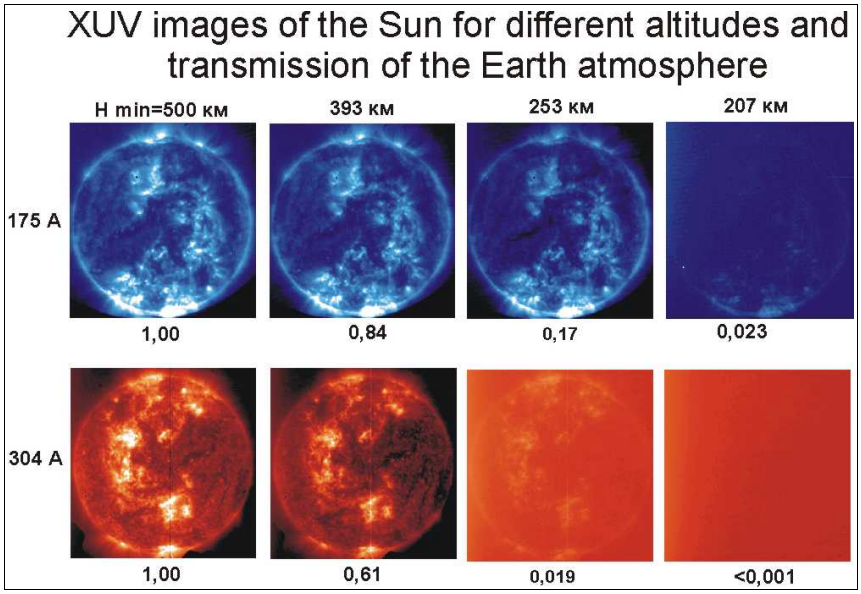

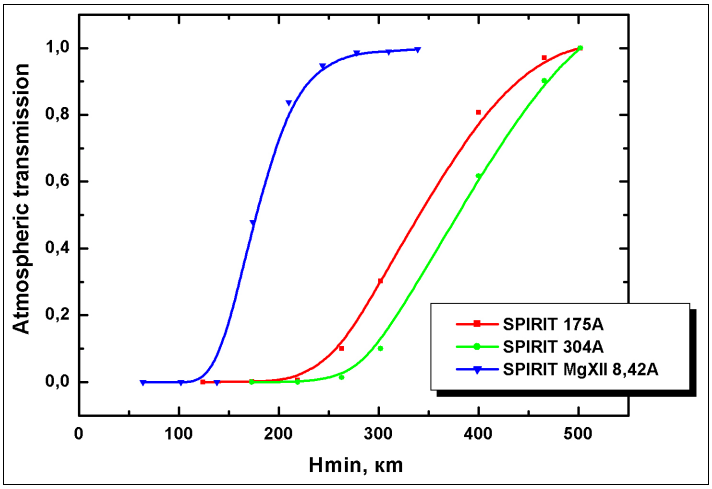

Fig. 34. (a) Solar X-ray images and (b) transparency of the Earth's atmosphere as a function of height H_{min}

Space gamma bursts recorded with the HELIKON gamma-spectrometer

In addition to the solar observations, the gamma-spectrometer HELIKON on board the "CORONAS-F" mission was recording space gamma bursts. On December 27, 2004, it recorded a unique event — the lunar echo of a giant gamma burst from a neutron star situated deep in our Galaxy at a distance of tens of thousands of light years. It was the fourth case when such a giant gamma burst was recorded since the appearance of the extra-atmospheric gamma astronomy in the 1960-ies. The direct signal from such a gamma burst has a tremendous intensity, which is far beyond the measuring ability of any existing detector. Therefore, we cannot determine the time profile of the burst and estimate the energy of explosion on the neutron star. The CORONAS-F mission was screened by the Earth from the direction to the gamma bust source and, hence, could measure the reflected signal attenuated by a factor of 50000. According to the preliminary estimates, the energy of explosion on the neutron star was about 10^{44} erg, exceeding significantly the total optical emission from one hundred billion stars of our Galaxy. It was the first in the world practice observation of the space gamma burst reflected from a celestial body or, in other words, the first case of location of a celestial body with the aid of a natural super-powerful gamma-radiation pulse.

Conclusion

During the operation period of the CORONAS-F satellite:

• a unique archive was build up comprising more than one million spectral images of the Sun and solar corona;

• multiple spectroscopic measurements made it possible to identify new spectral lines; the absolute content of various elements in the solar corona was determined for the first time; new methods of diagnostics of astrophysical plasma were developed;

• unique data were obtained concerning the X-ray, UV, gamma, and corpuscular emissions from solar flares and their effect on the Earth's magnetosphere, ionosphere, and atmosphere.

• the observation results were brought together to form voluminous catalogues and archives of data, which will serve the source of information for future research in the field of solar-terrestrial coupling and for planning new experiments.

3.4.2. EARTH AND SOLAR PHYSICS

3.4.2.1. Multispacecraft exploration of the ion acceleration in magnetosphere. Multiplet structure of the acceleration processes

The processes of non-adiabatic ion acceleration occurring in the vicinity of magnetic X-line produce highly accelerated (up to 2500 km/s) field-aligned ion beams (beamlets) with transient appearance streaming earthward in the Plasma Sheet Boundary Layer (PSBL) of magnetotail. An appearance of beamlets in the

PSBL, their velocity distributions and spatial-temporal scales reflect the features of ion acceleration sources in the magnetotail Current Sheet (CS). We have studied beamlets in two ways: statistical analysis of beamlet occurrence frequency and their spatial distribution over the Neutral Sheet (NS) and the case studies. According to the previous findings, beamlet occurrence frequency does not depend on the level of geomagnetic activity, but it may depend on the direction of Interplanetary Magnetic Field (IMF). It might be true because beamlets are accelerated in the distant parts of the magnetotail current sheet and correspondingly interplanetary conditions (not substorm activity since it develops closer to the Earth) should affect effectiveness of beamlet generation. Thus the statistical analysis was intended to understand if the IMF prehistory affects beamlet occurrence frequency and their spatial distribution observed in the magnetotail. Beamlet occurrence frequency and their spatial distribution over the Neutral Sheet (NS) were studied for the different IMF directions (IMF clock-angles) and separately for three magnetotail sectors: midnight sector ($|Y_{GSM}|< 7$Re), dawn and dusk flanks. This analysis was made on the base of Interball-1 beamlet observations (~500 events) obtained during the period 1995–1998.

The following main results were obtained:

1) Beamlet occurrence frequency in the magnetotail depends on the prehistory of interplanetary conditions, in particular, on the mean IMF clock-angle averaged over a period of at least 1 hour before the observation of beamlet. Moreover this dependence is different for the midnight sector of the magnetotail and for its flanks:

- in the midnight sector beamlets are observed for almost all directions of the IMF. During the periods of strong northward IMF beamlet occurrence frequency is considerably lower than for other IMF directions;
- during the periods of strong northward IMF no beamlets are observed at the flanks;
- beamlet occurrence frequency at the flanks is maximal when the IMF has strong B_Y component.

A sharp decrease of beamlet occurrence frequency has maximum for the periods of strong northward IMF. This feature is observed at all three sectors of the magnetotail, probably, because the dawn-to-dusk electric field which accelerates beamlets is weak for northward IMF direction. This result confirms the theory prediction that this electric field plays a main role in ion acceleration in the distant current sheet.

2) The spatial distribution of beamlets above the NS also depends on the mean IMF direction:

- at a preferentially southward IMF beamlets in the midnight sector are observed at altitudes of no more than 5Re (in the Z_{GSM} direction) above the NS, whereas at a preferentially northward IMF the beamlet are observed at greater altitudes (up to 10Re) above the NS;

- when the IMF has a strong B_Y component the spatial distributions of beamlets at dawn and dusk flanks are different. For the periods of $B_Y^{IMF}>0$ at the dawn flank beamlets are mainly observed at low altitudes (< 2Re) above the NS while at the same time at the dusk flank beamlets are observed at higher altitudes (3–5Re) above the NS; for $B_Y^{IMF} < 0$ the situation is opposite: the beamlet occurrence frequency at the dawn flank increases with height (beamlets are observed up to 10Re) above the NS while the frequency of beamlet observation at the dusk flank reaches its maximum near the NS.

The asymmetry in beamlet spatial distributions at flanks observed for the periods of strong B_Y component is probably caused by the presence of magnetotail convection along Y during these intervals. Due to this convection beamlets observed far at the flanks should have the sources located in the current sheet at different distances from the Earth.

Unfortunately, one-point Interball data do not permit to distinguish spatial and temporal effects and to study the spatial structure of beamlets. So we performed the detailed analysis of CLUSTER measurements in the PSBL of magnetotail. This analysis included reconstruction of beamlet structure (by using magnetic field and cold ion velocity variations observed in the course of beamlet propagation) and timing of the start-end points of individual beamlet registration at each of CLUSTER spacecraft.

The following main results were obtained:

1) beamlets are the spatial structures which are modified by the Alfven waves propagating earthward. In the analyzed cases beamlets were observed during the time interval ~10-15min. So the minimum time of their acceleration in the magnetotail may be more than 10min. The analysis of CLUSTER simultaneous observations of beamlet provides an estimate of its spatial scales. Beamlet is elongated along the magnetic field: its longitudinal size (several tens of the Earth's radii) is much larger than its transverse size (<1Re). This is one more piece of evidence that beamlet is generated in the spatially localized site in the current sheet of the distant magnetotail;

2) it was supposed before that beamlets are the structures extended along the straight-line magnetic field lines but the multi-point CLUSTER observations reveal that the magnetic field lines containing beamlet are bended so the beamlet has a "snake-like" spatial structure. Such a structure may be formed due to the development of a fire-hose instability which arises when a beamlet leave the current sheet at the site of its generation in the distant part of magnetotail. Using the maximum value of the magnetic field for which the fire-hose instability conditions are still satisfied the lower bound of the distance from the Earth to the beamlet sources can be estimated. Case studies show that its value is about 80Re.

Moreover, Cluster high-resolution measurements of beamlet velocity distributions provide, for the first time, experimental evidences of the resonant character of beamlet acceleration. Earlier kinetic model attributed the filamentary and/or bursty manifestations of these processes to current sheet resonances and predicted the scaling law for the velocity of subsequent beamlet structures as

$V_N \sim N^{2/3}$ (here V_N is the ion parallel velocity of the N-th structure). However experimental evidences in favor of these predictions are scarce. One of the reasons is that most observations are made near the Earth where ion beams produced by different sources overlap and resonance structures are generally smeared in ion distributions. On the basis of Cluster observation in the PSBL of magnetotail we find experimental observations of "double-peaked" ion distributions produced by ion beams accelerated by at least two different resonant processes operating at spatially separated sites in the CS (see Fig. 1). The simultaneous observations in the near-Earth PSBL of ion multiplets consisting of, at least, two field-aligned ion beams with distinct parallel velocities (up to two times) provide an evidence of the simultaneous operation of different acceleration sources in the magnetotail CS. We have analyzed 100 "double-picked" beamlet velocity distribution functions and statistically proved the predicted scaling law for quiet and moderately disturbed periods. It seems that such a scaling law has "universal" character since it does not depend on any model of the magnetic field in the CS.

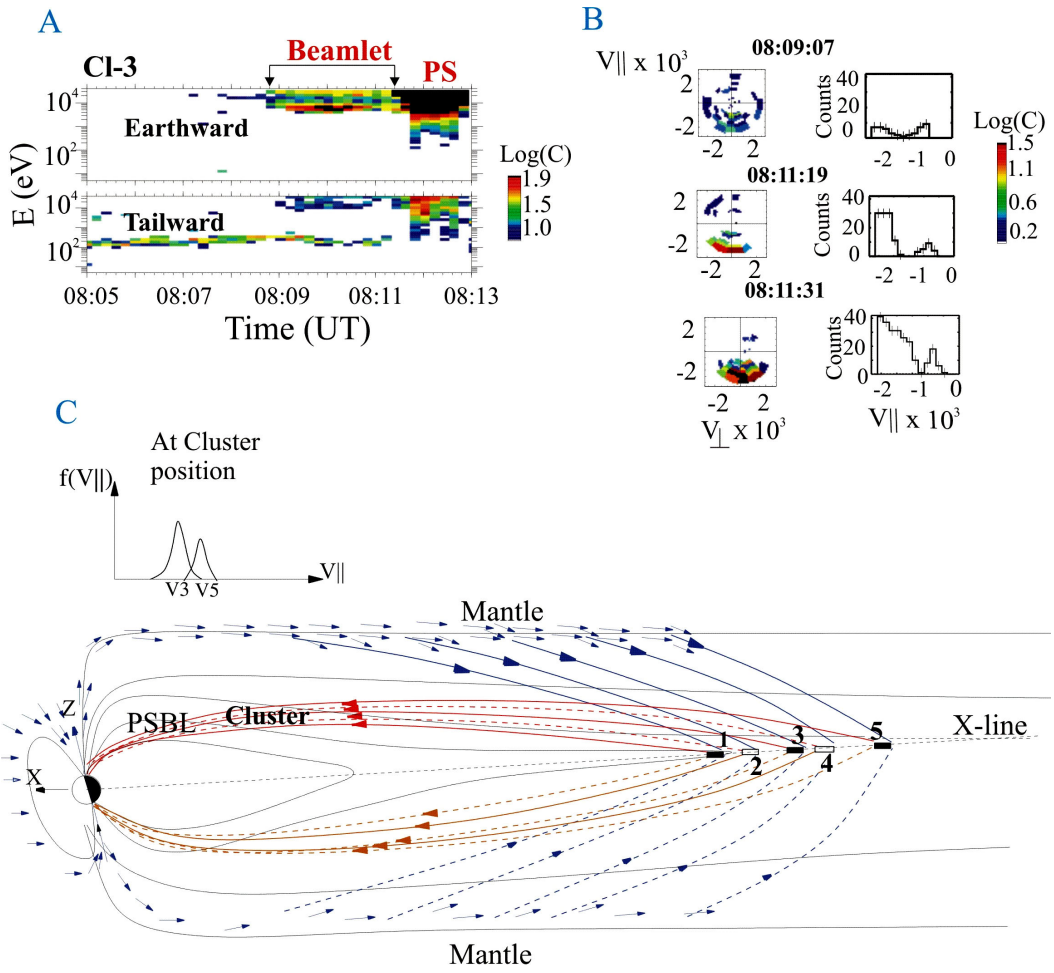

Fig. 1. A: Energy-Time spectrogram of ions measured on 01.09.2003 by Cluster at PSBL of magnetotail. Two beamlets with energies ~ 5keV and 30 keV are clearly observed. B: Left Column: Set of 2D-ion velocity distribution functions in plane (Vper, Vpar). Right Column: 1-D cuts of velocity distribution functions along the magnetic field. Two picks of distribution corresponding to two beamlets are clearly observed. C: Illustration of beamlet resonance acceleration in the CS and "double-picked" velocity distribution formation near the Earth

3.4.2.2. Theoretical modeling of self-consistent thin current sheets in the Earth's magnetosphere

Current sheets are one of the key elements of the Earth's magnetosphere, determining the magnetic energy storage and release. An analytical self-consistent model of multicomponent thin current sheets, where the plasma consists of ions of both solar wind and ionospheric origin, is presented. The influence of the electron population is taken into account assuming Boltzman-like quasi-equilibrium distribution in the electrostatic field, which can lead to a sharp peak in the electron current density in the center of the current sheet. We include the contribution of non-adiabatic O^+ ions in our model as one of the terms in the Grad–Shafranov-like system of equations describing the quasi-equilibrium configuration. It is shown that the contribution of oxygen ions to the total cross-tail current usually does not exceed 30 % for realistic conditions (Fig. 2), but current "wings" carried by O^+ ions produce significant broadening of the current profile (Fig. 3). The model is in agreement with Cluster and Prognos observations, where the current across magnetotail during substorm is carried partially by heavy ions from ionosphere and the resulting thicknesses of current sheets are about $(1.5–3)\cdot10^3$ km, i.e. longer than the proton gyroradius.

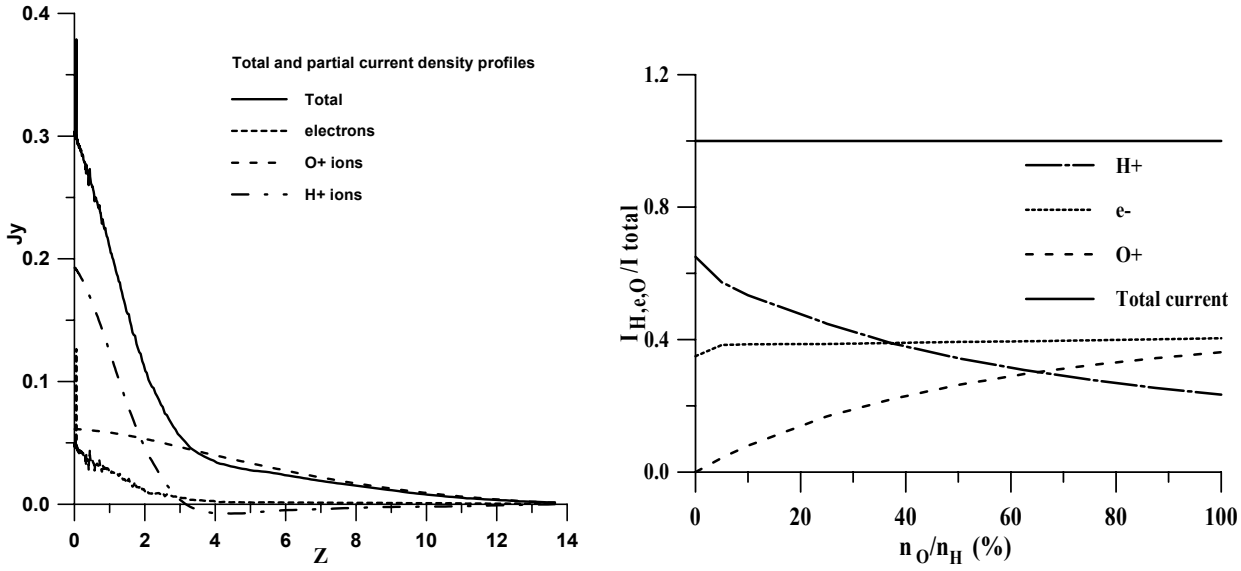

Fig. 2, 3. The contribution of ions O^+ and H^+ in the total current depending on the ratio of concentrations of O^+ and H^+ ions (1) and distribution of currents of O^+ and H^+ ions across the magnetosphere tail (2)

3.4.2.3. Oscillatory magnetic flux tube slippage in the plasma sheet

Cluster observations in the magnetotail revealed abundance of strongly inclined current sheets. We determine magnetic configuration of a particular subset of such phenomena: series of sheet crossings, having significantly differing inclinations of consecutive events and occurring during quiet conditions. These

wave-like variations appear to propagate azimuthally, their magnetic amplitude and magnetic gradient (current density) inside the sheet are proportional to their steepness (degree of inclination). In spite of significant up to 150° normal direction changes between neighboring crossings, magnetic field direction inside neutral sheet remains almost constant. The wavelengths and spatial amplitudes are of the order of 2—5 R_E. This phenomenon is subsequently interpreted as a quasi-periodic (in our cases) almost vertical slippage motion of the neighboring magnetic flux tubes in the high-beta plasma sheet, rather than large-scale flapping.

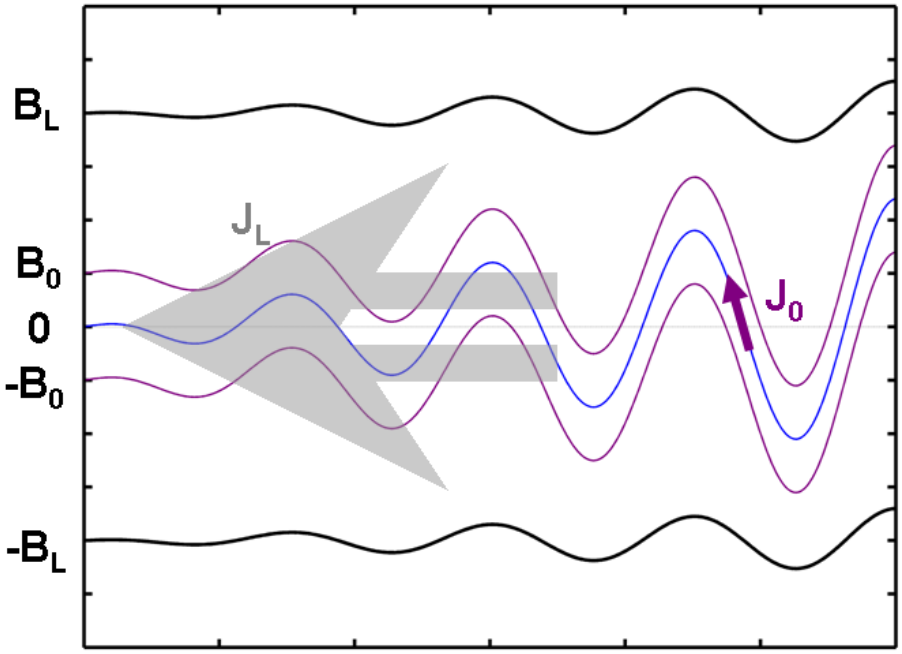

Fig. 4. The scheme of dynamic sheet modification. See text for details. The thin variable current layer J_0 creates the magnetic wave $\pm B_0$, observed by a spacecraft as a series of sheet crossings. The full magnetic gradient $\pm B_L$ is supported by much thicker horizontal current J_L

3.4.2.4. The properties of the solar wind discontinuities from simultaneous observations by five spacecraft (INTERBALL, WIND, ACE, GEOTAIL, IMP8)

The study is based on the magnetic field carried out onboard the five spacecraft: INTERBALL, WIND, ACE, GEOTAIL и IMP8 orbiting simultaneously in the solar wind in 1998–1999. The discontinuities unambiguously identified with the magnetic field data gathered by each of five spacecraft has been selected and, then, analysed. It is shown that in overwhelming number of events the current sheet (tangential discontinuity with magnetic field parallel to its surface both upstream and downstream sides) is the best approximation to observations. Geometry of the fronts is found to be planar (the radius of curvature typically exceeds 400Re; Re, Earth's radius, is of about 6380 km), discontinuities are "frozen" in the solar wind and are convected by its flow. The angle between Sun-Earth line and surface normal constitutes, in average, 36 deg.

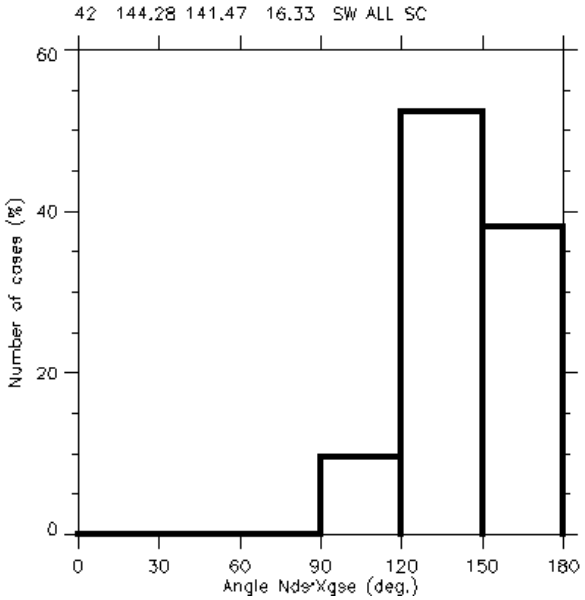

Fig. 5. Solar wind discontinuities, angle between the Sun direction and normal of discontinuity front. The average value is about 36o with respect to the Sun-Earth line

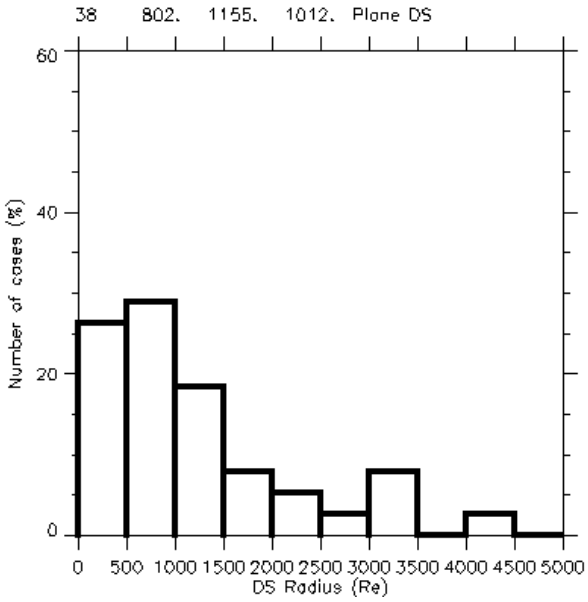

Fig. 6. Solar wind discontinuities, their radii of curvature estimated with the model of inflated spherical front. The typical values exceed 400Re, i.e. the fronts are practically planar

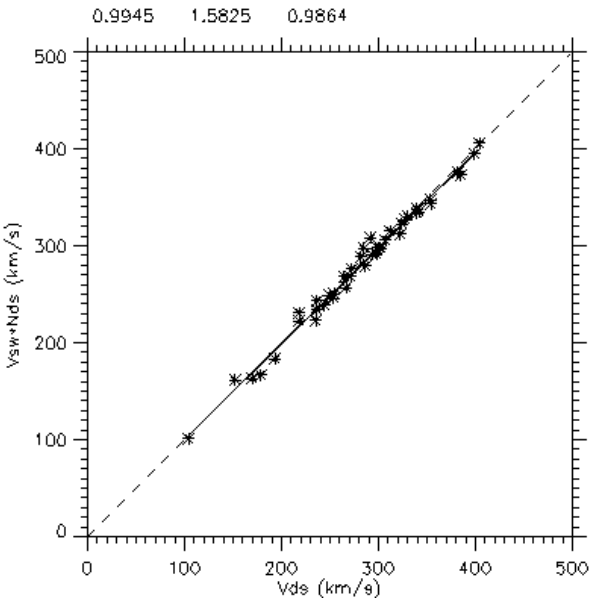

Fig. 7. The propagation velocity of discontinuity estimated with the triangulation method versus projection of the solar wind bulk speed on the discontinuity normal. Both values practically coincide which implies the convection of the discontinuity by the solar wind flow

3.4.2.5. The extensive experimental material concerning extremely active phenomena in October-November, 2003 and in November, 2004 is collected and analysed

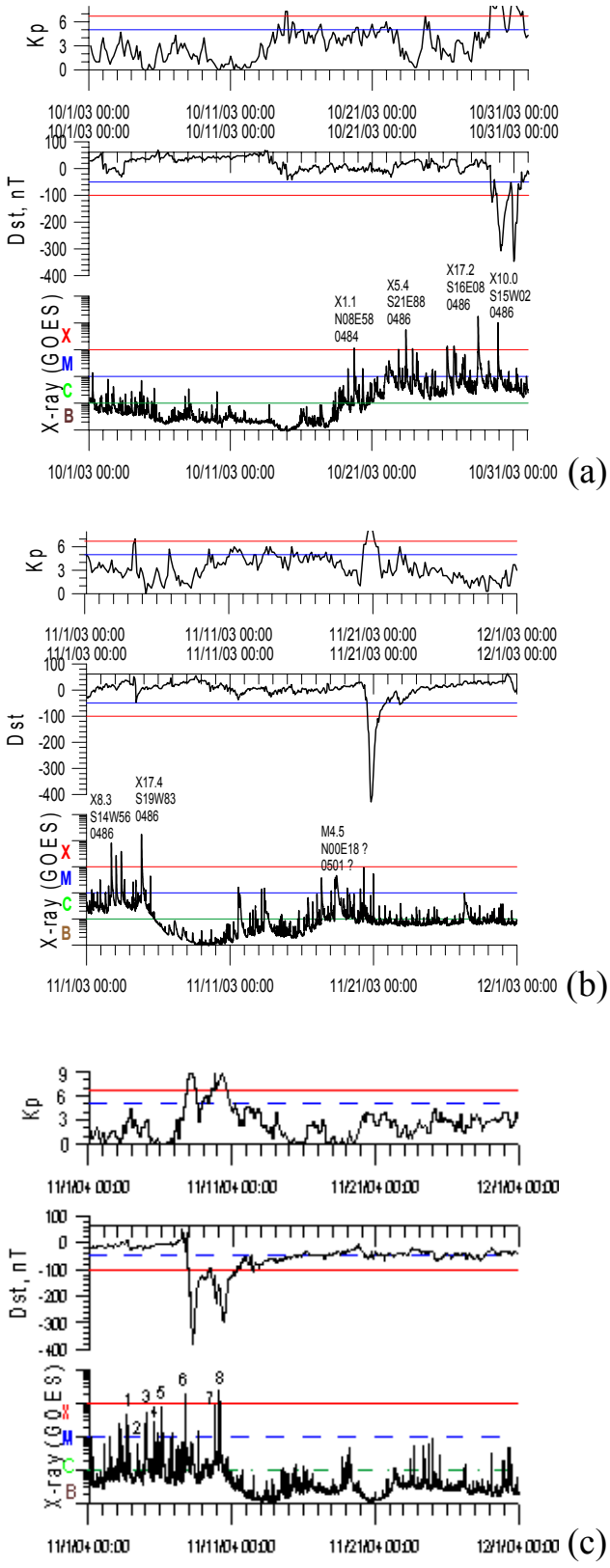

Fig. 8. Sequence of solar and ground measurements in October-November, 2003 and October, 2004. Top and average panels: Kp and Dst indexes (dark blue and red lines specify borders of the moderate and strong magnetic storms)

This material has been obtained, basically, by domestic researchers (more than 60 scientists from more than 10 scientific organizations of the Russian Federation). It consists of observation of the Sun (S/C KORONAS-F, SOHO, GOES, RATAN-600 both group of optical and radio telescopes), a heliosphere (S/C ACE, WIND, Ulysses and instrument HEND on S/C Odessey) and magnetosphere and ionospheres of the Earth (S/C KORONAS-F, Express-A2 and A3, Meteor-3M, and also a wide network of magnetic and geophysical stations and neutron monitors). As it is well seen in Fig.8, during 16 days (beginning on October, 19th) in 3 active areas on the Sun has occurred 16 greater flares, 11 of which had X-ray class X. One of them (on November, 4th) has led a level higher than limit of x-ray instrument at level X17.2. The magnetic storm on October, 30th has reached magnitude Dst = –401 nT. When these active areas have returned in 2-nd half of November on the visible party of the Sun, they have shown rather small flare activity, however on the Earth there was 2-nd for all history of measurements a magnetic storm with Dst = –472 nT. Later year after extreme events on the Sun, in a heliosphere and on the Earth in October-November, 2003 the similar situation has repeated in November, 2004 (see Fig. 8). In work the basic observation data concerning by the period when on the Earth the strong magnetic storm with Dst = –373 nT was observed are analyzed. Taking into account of a number of parameters (level of disturbances on the Sun, in solar wind and magnetosphere) the considered period concedes to the similar period of 2003, nevertheless, cited data testifies that owing to events of falls of 2003 and 2004 the declining phase of 23-rd solar activity cycle is one of the most active for all period of comprehensive investigations of solar-terrestrial links.

3.4.2.6. Dependence of O^+ ionospheric ions outflow in the polar cap on polar rain intensity

On the basis of TYPERBOLOID and ION instrument data installed on INTERBALL-2 satellite comparison of ionospheric ion outflows (polar wind) with weak electrons fluxes (polar rain) was done in the polar cap at altitude ~20000 km.

Pains to exclude ionospheric ion fluxes with additional energization were taken. Consequently fluxes of “cleft ion fountain” and auroral outflow were excluded from the analysis and only hypothetical polar wind fluxes were analyzed. In the summer times when polar ionosphere is fully light up it were detected by HYPERBOLOID instrument two different types of upgoing ion fluxes in the polar cap. First is characterized only by cold H^+ ions detecting while second is characterized by both H^+ and O^+ ions fluxes detected by the instrument. In the second type O^+ fluxes have sufficient velocity to overcome a positive satellite potential versus surrounding plasma. The number of occurrence these two types of outflow versus the polar rain intensity were investigated. It was found that there is dependence of O^+ ion outflow in the polar cap even on very weak polar rain.

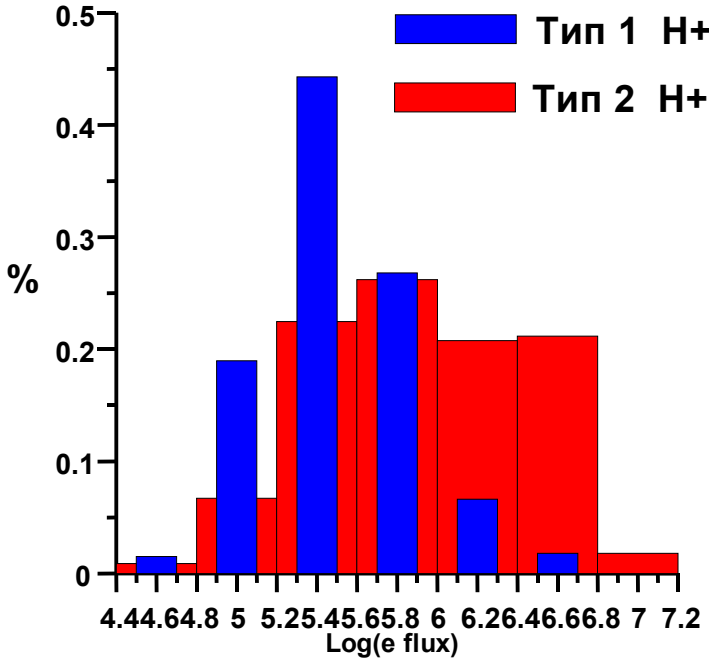

Fig. 9. The diagram shows the number of occurrence two detected different types of ionosphere plasma outflow versus polar rain electron flux. Type 1 (blue) — only H^+ ion fluxes were detected, O^+ fluxes are under sensitivity; Type 2 (red) — both H^+ and O^+ ions were detected

3.4.2.7. Solar energetic particle in the polar heliospheric regions

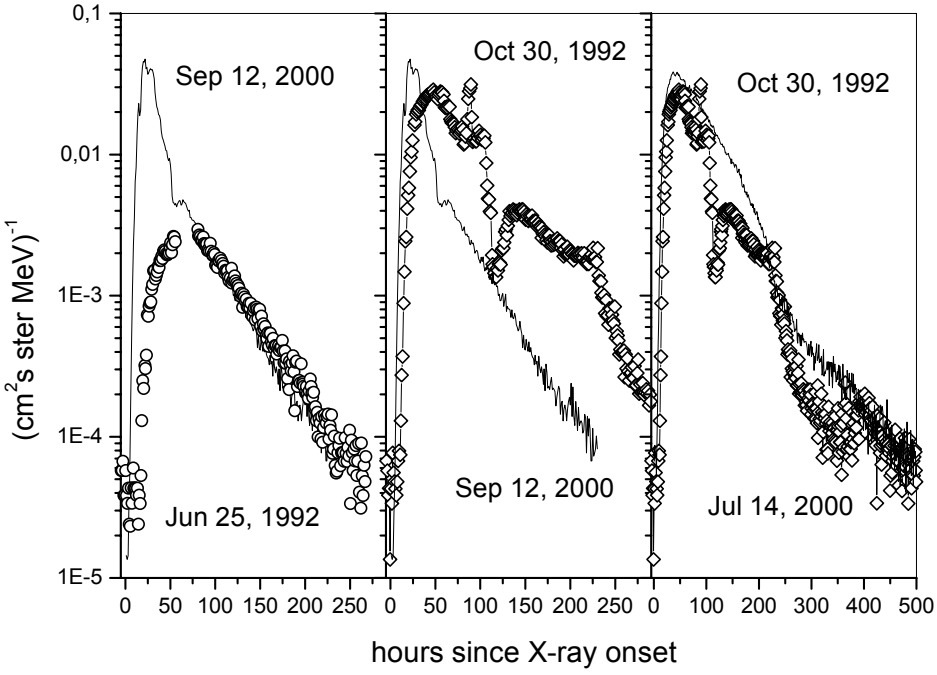

Fig. 10. Comparison of the polar SEP events (14 July and September 2000) with the in-ecliptic events at 5 AU (25 June and 30 October 1992) observed by KET/Ulysses

Observations of eight solar energetic particle (SEP) events in the polar heliospheric regions and six events near the Jupiter orbit were analyzed (>30 MeV,

KET/Ulysses). These events are easily identified with well-known episodes of the solar activity in 1992, 1997, 2000–2001 and 2003 and the corresponding SEP events near the Earth (GOES). Analyzing the diversity and similarity of these SEP events we conclude that the Sun should be a source of SEP prolonged in space and time, much more complex than assumed before. Very similar intensity time profiles observed during the first 2-3 days of some events indicate the same averaged mechanism of SEP propagation to distant locations in the heliosphere. Later, when spatial gradients are weak or non-existing in the heliosphere (the reservoir effect), the events are different from each other reflecting total number of particles injected into the heliosphere, a rate of particle escape from the storage region and a local modulation by solar wind disturbances.

3.4.2.8. Electron observations in the Low latitude boundary layer (LLBL) by Interball Tail satellite

Electron observations on February 15, 1996 in the Low latitude boundary layer (LLBL) by Interball Tail satellite under southward-duskward magnetosheath magnetic field showed that the parallel electron velocity distribution is changing self-consistently with varying number density in the LLBL. Namely, the shape of parallel velocity distribution does not change in log-log scale indicating that electron parallel velocities increase in the same proportions as the number density in the LLBL decreases. This indicates the conservation of the second magnetic invariant within “closed” magnetic structures and possible role of Fermi acceleration within LLBL. Characteristics of electrons within LLBL suggest the existence of closed magnetic topology and supports multiple reconnections between magnetosheath and magnetospheric flux tubes with the formation of spiral magnetic flux tubes. This implies that the multiple reconnection is at times an important factor in the formation of LLBL.

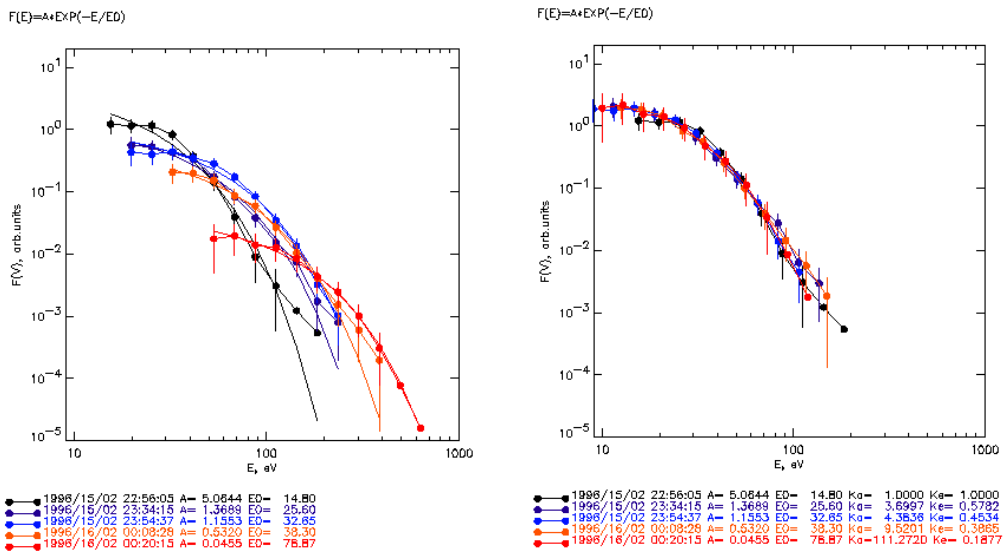

Fig. 11. Measured electron spectra (left) and fitted to each other (right)

3.4.2.9. Solar Wind Exploration

The solar wind variability was investigated in the frequencies range 10^{-3}…1 Hz. Histograms of ion flux and magnetic field magnitude and the relative standard deviations of fluctuations of these parameters were obtained on the very large statistics using the systematic measurements by the instruments onboard the Interball-1 spacecraft in the range of high frequencies which has not been investigated before in detail.

On the base of analysis of these data it was shown that, on the average, the relative variations of the both ion flux and magnetic field magnitudes are about 10% of the background value at the low frequencies (10-3 - 10-2 Hz) and about 3% at higher frequencies (10^{-2}…1 Hz).

These results in the part of statistics of magnetic field variations were also compared with similar analysis of Cluster magnetic field measurements and they correspond to each other rather well.

From these data the relationship was obtained between levels of plasma and magnetic field variations in the regions of undisturbed solar wind, foreshock and magnetosheath. For both low and high frequencies the amplitudes of variations in foreshock and magnetosheath regions are considerably larger (on the average, about 3 times) than in the undisturbed solar wind.